# Using mixed-clay sediment gravity flow rheology as an indicator for flow velocity and run-out distance

**Megan L. Baker[1], Jaco H. Baas[2], Jonathan Malarkey[2] and Ricardo Silva Jacinto[3]**

[1] Department of Geography, Durham University, Durham, UK

[2] School of Ocean Sciences, Bangor University, Menai Bridge, Isle of Anglesey, UK

[3] Geo-Ocean Unit, IFREMER Centre de Bretagne, Plouzané, France

**Keywords: sediment gravity flow, clay minerals, rheology, cohesion, yield stress**

**Abstract**

It is important to determine if the dynamics of mixed-clay sediment gravity flows can be predicted from their dominant clay type, because natural gravity flow deposits can contain mixtures of clay minerals of different cohesive strength, and latitudinal zonation in clay mineral production may influence depositional patterns in mud-rich submarine fans. The present lock-exchange experiments produced high-density sediment gravity flows carrying different proportions of strongly cohesive bentonite clay and weakly cohesive kaolinite clay with a fixed 20% volumetric concentration. Head velocity and run-out distance of the flows reduced, and starting suspension yield stress increased, as bentonite fraction increased beyond 20%. However, for bentonite fractions ≤ 20%, the initial suspensions had lower yield stresses and the flows were more mobile than the pure kaolinite flow, implying small bentonite fractions reduce the cohesive strength of the suspensions. Predictive equations for mixed-clay suspension yield stress, and head velocity and run-out distance of mixed-clay flows, based on yield stresses of pure-clay constituents, indicates minimal interaction between the constituents for bentonite fractions ≤ 20% and increasingly non-linear interactions for bentonite fractions > 20%. These results suggest natural sediment gravity flow dynamics and deposits may be sensitive to the most cohesive clay rather than the dominant.

## 1 Introduction

Sediment gravity flows (SGFs) transport large volumes of sediment to the deep ocean, thus forming the largest sediment accumulations on our planet, called submarine fans (Talling, 2014). Closely linked to the external controls of tectonics, climate, and sea level, a prime control on the size and depositional style of submarine fans is sediment supply, which includes the amount and composition of the sediment (Stow et al., 1996). For example, submarine fans mainly composed of mud, the most abundant sediment type on Earth (Hillier, 1995), are generally of a greater size than fans predominantly composed of sand (Reading & Richards, 1994). The behavior of mud-rich SGFs is complex due to the ability of clay minerals to modulate SGF behavior via cohesive forces between particles, which in turn influences the depositional properties of these flows (Baas et al., 2009, 2011; Baas & Best, 2002; Wang & Plate, 1996). A greater understanding of clay-rich, cohesive SGFs is required to reconstruct the depositional patterns observed in modern and ancient mud-rich submarine fan systems, as well as the mud-rich outer fringe of sandier deep-marine systems.

Clay can greatly influence SGF dynamics and deposits owing to its cohesive properties, which allows suspended clay particles to bind together via attractive Van der Waals forces to form flocs and gels (Winterwerp & Van Kesteren, 2004). The formation of clay flocs and gels can modulate the turbulent forces within cohesive SGFs to produce transitional flows with unique behavior intermediate between fully turbulent and fully laminar flows (e.g., Baas et al., 2009). Laboratory experiments have shown that the cohesive properties of cohesive SGFs depend on the clay concentration and clay mineral type, along with other factors, including the biological cohesion and the ratio of cohesive to non-cohesive sediment (Baas et al., 2009; Baker et al., 2017; Baker and Baas, 2022; Craig et al., 2020; Hermidas et al., 2018: Ilstad et al., 2004; Marr et al., 2001).

For example, Marr et al. (2001) contrasted sand-rich SGFs containing strongly cohesive bentonite clay and weakly cohesive kaolinite clay in the laboratory. For flows of the same sediment concentration and ratio of sand to clay, those containing kaolinite had longer run-out distances than those containing bentonite. The large differences in behavior between the kaolinite and bentonite flows can be attributed to the different chemical and physical properties of clay minerals (Marr et al., 2001; Hillel, 2003). Clay minerals have different shapes, sizes, layer charges, cation exchange capacities, edge charge densities, and particle edge structures, which control the strength of the attractive forces between individual clay particles in the suspension (Lagaly, 1989). There is a general trend in the cohesive strength of the common clay minerals: kaolinite and chlorite are generally considered to be weakly cohesive, illite is considered to be moderately cohesive, and smectite (which includes bentonite) is considered to be strongly cohesive (Fig. 1a; Hillel, 2003; Holtz & Kovacs, 1981; Yu et al., 2014).

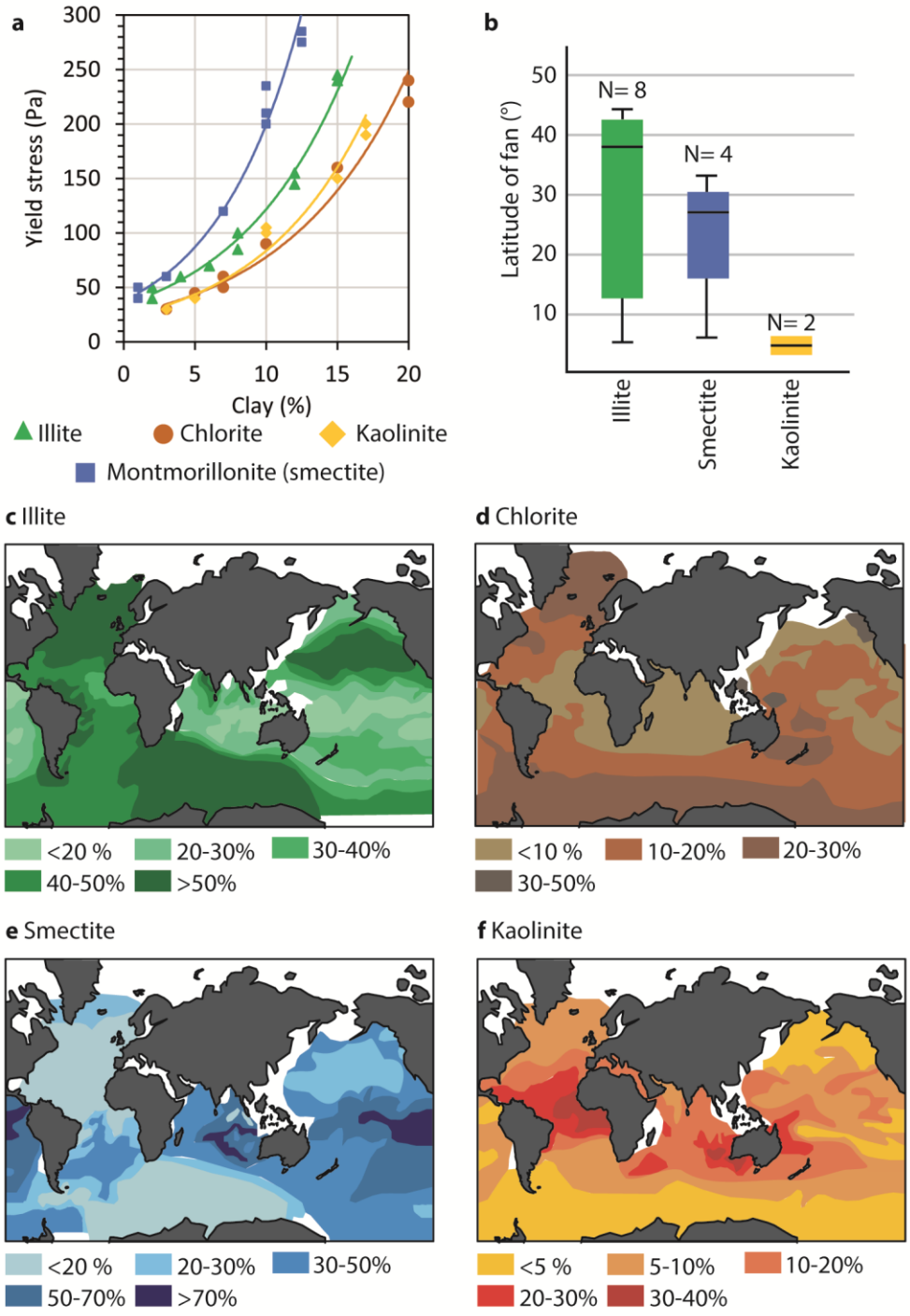


***Figure 1**: Different clay minerals have different cohesive strengths and are produced in distinct climatic zones, which may influence the dominant clay type and depositional patterns in mud-rich submarine fans. (a) Yield stress of subaerial debris flows composed of gravel, sand, and clay at a*

*fixed volume concentration of solids of 58%. As the clay fraction in the suspension increases, the yield stress increases. The rate of increase in yield stress reduces from montmorillonite, via illite, to kaolinite and chlorite. Redrawn from Yu et al. (2014). (b) Latitude of submarine fan (defined as the average of the latitudinal extent of the fan) against dominant clay mineral type. From Baker (2020). (c–f) Latitudinal distribution of illite (c), chlorite (d), smectite (e), and kaolinite (f) in the < 1 μm fraction of surficial modern deep-marine sediment. Percentage values refer to the relative clay abundance in the < 1 μm fraction. Adapted from Fagel (2007).*

Present understanding of the importance of clay mineral type on SGF behavior is limited to experiments comparing flows containing single clay mineral types (Baas et al., 2016; Baker et al., 2017; Marr et al., 2001). However, in the natural environment, the deposits of clay-rich SGFs are usually composed of a mixture of different clay minerals, based on a limited number of SGF deposits where clay mineral type has been determined (Alonso & Maldonado, 1990; France-Lanord et al., 2016; Kolla et al., 1980; Zhang et al., 2015). The contrasting cohesive strengths of different clay minerals, and their possible interactions, will change the cohesive properties of mixed-clay SGFs, which in turn may influence the deposits of these flows. Laboratory experiments are required to help understand how mixtures of common clay mineral types control the cohesive forces of clay-rich SGFs.

Interestingly, although SGF deposits in natural environments contain a mixture of clay minerals, there is a distinct latitudinal pattern in the dominant clay mineral type in recent deep-sea surface sediment (Biscaye, 1965; Chamley, 1986; Griffin et al., 1968; Rateev et al., 1969, Fig. 1c–f). This latitudinal zonation of clay minerals is thought to be related to the contemporary climates on the continents. Climate controls the intensity of physical and chemical weathering, and these weathering processes to a large extent dictate the type of clay minerals formed (Biscaye, 1965;

Chamley, 1981; Griffin et al., 1968; Fagel, 2007; Thiry, 2000, Fig. 1c–f). However, many other factors also control clay mineral formation, including composition of source rock, relief of the land, and authigenesis, which can confound the relationship between clay minerals and climate. Of the common clay mineral types, kaolinite is abundant in equatorial sediment, whereas chlorite is typically found in the polar regions of the world (Griffin et al., 1968, Fig. 1d,f). Illite and smectite have less distinct distribution patterns (Fig. 1c,e). However, illite can generally be found in moderate to high latitudes, whereas smectite is commonly located in tropical to moderate latitudes (Griffin et al., 1968; Chamley, 1989; Thiry, 2000; Fagel, 2007). This climate-controlled, latitudinal zonation of dominant clay minerals with different cohesive properties could influence the flow behavior of cohesive SGFs and ultimately feed into the depositional patterns and geometry of mud-rich submarine fans. However, since cohesive SGFs are rarely composed of a single clay type, there is a need to understand if the behavior of clay mixtures can be predicted from the dominant clay type in the flow or if the relative contribution of the different clay types is required. If relative contributions need to be considered, the question then is if these contributions are proportional, or disproportional as a result of physical-chemical interaction between the clay types.

The cohesive strength of clay flows can be quantified via rheological parameters rather than by their clay mineral composition and concentration. These parameters include the suspension yield stress and shear modulus, which measure the strength of the attractive interparticle forces, i.e., cohesive bonds, between clay particles (Au & Leong, 2013; Lin et al., 2016), and the apparent viscosity, which measures the resistance of the fluid to flow (Mezger, 2006). Experiments have shown that the yield stress of the starting suspension can predict the dimensionless maximum head velocity and the run-out distance of pure-clay SGFs (Baker et al., 2017), thus demonstrating that

the rheology of single-clay SGFs can aid understanding of, and predict, their flow behavior and deposits.

The present study uses laboratory experiments to investigate how changing the ratio of strongly cohesive bentonite and weakly cohesive kaolinite in cohesive SGFs changes the flow dynamics and deposits, to further our understanding of mixed-clay SGFs in the natural environment. The specific objectives of this research were:

1. to determine how changing the proportions of bentonite to kaolinite in mixed-clay SGFs at a fixed total concentration influences the flow velocity, run-out distance, and deposit geometry;
2. to quantify the rheological properties of these mixed-clay starting suspensions and relate these to the observed changes in flow behavior;
3. to investigate if the yield stress of mixed-clay suspensions can be accurately predicted from the combination of the yield stresses of the pure-clay components, and if predictive equations linking yield stress to flow behavior for pure-clay SGFs can be applied to mixed-clay SGFs;
4. to discuss how these results can be used to improve predictions of the flow dynamics and deposit properties of natural mixed-clay SGFs.

## 2 Materials and Methods

### 2.1 Lock-exchange flume-tank experiments

Ten SGF experiments were conducted in a 5-m long, 0.2-m wide, 0.5-m deep, and 0°-slope, smooth-bottomed lock-exchange tank (Fig. 2), following the experimental methods described in Baker et al. (2017). A suspension of clay and seawater (filtered from the Menai Strait, NW Wales, UK) filled a 0.31-m long reservoir to a depth of 0.35 m. A lock gate separated the reservoir from

the main compartment of the tank, which was filled with seawater to the same depth (Fig. 2). The lock gate was then lifted to generate the SGF. The SGF suspension in the reservoir had a fixed volume concentration of 20%. The sediment suspension was composed of a mixture of strongly cohesive bentonite and weakly cohesive kaolinite, expressed as the fraction of bentonite in the flow, $b$, which varied between 0% and 100% (Table 1, where $1–b$ is the fraction of kaolinite). The kaolinite had a median particle size, $D_{50,}$ of 9.1 μm and was supplied by Imerys Ltd. The bentonite was composed of Na-montmorillonite with a $D_{50}$ of 5.6 μm and was supplied by RS Minerals Ltd.

To account for any time-dependent cohesive properties of the clay minerals, a consistent method was used to prepare the suspension. First, half of the seawater and sediment was mixed in a cement mixer for 15 minutes, before the remaining material was added and mixed in for another 15 minutes. The mixture was then poured into a container and mixed with a handheld cement mixer for a further 10 minutes. The fully-mixed suspension was then progressively added to the reservoir with the lock gate in place while the tank filled with seawater. The suspension in the reservoir was mixed using the handheld mixer for 60 s and then given *c.* 10 s to come to rest before lifting the gate and generating the SGF.

As the flow travelled along the tank, a high-definition video camera tracked the flow front (Fig. 2). The velocity of the head of the flow was calculated using the time-stamped video frames and scale at the bottom of the tank. Flow run-out distances, defined as the maximum extent of the deposit from the lock gate, were recorded for all flows that stopped before reaching the end of the tank. For flows with a measurable run-out distance, the height of the SGF deposit with distance along the tank was measured using a SeaTek 5 MHz Ultrasonic Ranging System, which uses the two-way travel time of an ultrasound pulse to determine the vertical distance to the deposit top.

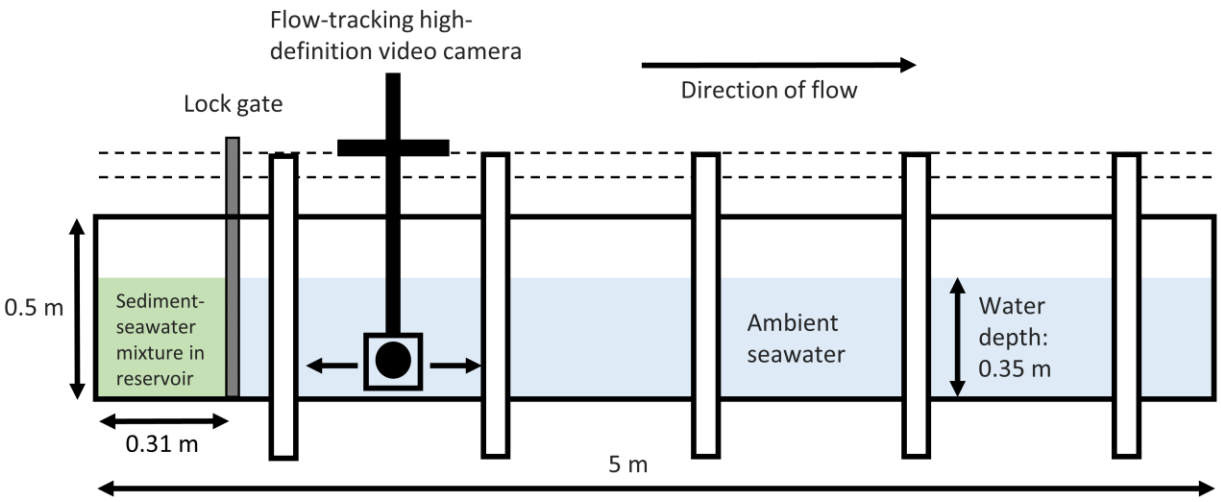


***Figure 2**: Schematic side view of the lock-exchange flume. The tank is 0.2 m wide and the floor was set to a slope of 0°.*

***Table 1:*** *Collected data for the lock-exchange and rheology experiments, using suspensions with a fixed volume concentration of 20% and different fractions of bentonite, b, and kaolinite, 1–b. Oscillatory, strain and stress refer to the different rheological tests. HDTC = high-density turbidity current.*

| Run | Bentonite fraction, $b$ (%) | Kaolinite fraction, $1–b$ (%) | pH | Run-out distance, $x_0$ (m) | Maximum head velocity, $U_h$ (m $s^{-1}$) | Flow type | Yield stress (Pa) | | | Complex shear modulus (Pa) | | |
|---|---|---|---|---|---|---|---|---|---|---|---|---|
| | | | | | | | Oscillatory | Strain | Stress | Oscillatory | Strain | Stress |
| 1 | 0 | 100 | 4.3 | - | 0.43 | HDTC (weak) | 31.95 | 3.05 | 2.74 | 15.04 | 1.18 | 1.79 |
| 2 | 10 | 90 | 7.1 | - | 0.45 | HDTC (weak) | 17.85 | 2.72 | 2.48 | 8.00 | 1.01 | 1.74 |
| 3 | 20 | 80 | 7.3 | - | 0.45 | HDTC (weak) | 17.85 | 3.85 | 3.86 | 8.21 | 1.96 | 2.74 |
| 4 | 35 | 65 | 7.4 | 4.11 | 0.41 | HDTC (strong) | 21.25 | 7.39 | 7.44 | 12.11 | 3.56 | 5.59 |
| 5 | 45 | 55 | 7.6 | 3.46 | 0.38 | HDTC (strong) | 26.20 | 12.3 | 12.6 | 17.68 | 6.13 | 7.36 |
| 6 | 55 | 45 | 7.6 | 2.45 | 0.35 | HDTC (strong) | 28.42 | 17.8 | 19.4 | 23.76 | 10.41 | 11.61 |
| 7 | 65 | 35 | 7.8 | 1.80 | 0.32 | Mud flow | 50.80 | 30.6 | 36.8 | 39.57 | 18.44 | 17.09 |
| 8 | 75 | 25 | 7.9 | 1.07 | 0.25 | Mud flow | 71.60 | 47.6 | 52.7 | 51.80 | 24.64 | 28.74 |
| 9 | 85 | 15 | 8.0 | 0.78 | 0.17 | Mud flow | 106.90 | 65.6 | 71.4 | 69.57 | 29.58 | 37.41 |
| 10 | 100 | 0 | 8.2 | 0.22 | 0.07 | Slide | 217.3 | 102 | 104 | 122.34 | 39.63 | 63.30 |

## 2.2 Rheology experiments

The rheological properties of the mixed kaolinite–bentonite suspensions (of the same composition as the suspensions used in the lock-exchange experiments) were measured using an Anton Paar Physica MCR 301 rheometer at IFREMER (Brest, France), following the same experimental protocols as in Baker et al. (2017). These experiments were carried out at 20°C with a concentric-cylinder geometry using suspensions at a fixed 20% total volume concentration and varying the proportions of kaolinite and bentonite clay (Table 1). Each 200 $cm^3$ sample was prepared by weighing the required Menai Strait seawater and the two clay types in a plastic bottle. The bottle was then energetically shaken by hand for 10 minutes to produce a well-mixed suspension. Immediately before a subsample of the suspension was spooned into the rheometer cup, the sample was shaken for a further 30 seconds. Oscillatory, strain-controlled, and shear-controlled rheological tests were conducted using fresh subsamples for each suspension to derive the yield stress and the complex shear modulus.

In the oscillatory test, the inner cone rotation was ramped up logarithmically with an increasing oscillating strain from 0.0001 to 1000 $s^{-1}$ and the resultant stress, loss modulus, and storage modulus were measured. For the strain-controlled test, the strain rate was ramped up linearly from 0.0001 to 0.01 $s^{-1}$, and the resulting stress was measured at each time step. Finally, for the stress-controlled test, the stress was increased logarithmically from 0.0001 Pa to 3 times the yield stress recorded from the strain-controlled test, and the resulting strain rate of the suspension was measured. The agreement in trends of the rheological parameters derived from the different tests with changing fractions of kaolinite and bentonite was used to check the reliability of the results.

# 3 Results

## 3.1 Lock-exchange flume-tank experiments

### 3.1.1 Visual observations

Video recordings show that the $b$ = 0% to $b$ = 20% flows had pointed, semi-elliptically shaped heads, which hydroplaned at a distance from the lock gate, $x$, of *c.* 1 m to *c.* 4 m. The heads of the $b$ = 0% and $b$ = 10% flows initially had a uniform color and were visually dominated by turbulent mixing (Fig. 3a). However, by $x$ = *c.* 1.80 m the $b \leq 10\%$ flows could be divided into two zones: a dark lower zone 1 without visible internal mixing and a lighter upper zone 2, where ambient water mixed into the flow and Kelvin-Helmholtz instabilities developed. The head of the $b$ = 20% flow was dominated by turbulent mixing only at the start; from $x \approx 0.9$ m the flow could be divided into the two layers described above (Fig. 3b). Between $x$ = *c.* 1.5 m and $x$ = *c.* 3.5 m, linear features of clear ambient water, termed coherent fluid entrainment structures by Baker et al. (2017), were observed in zone 1 of the heads of the $b \leq 20\%$ flows (Fig. 3b). The coherent fluid entrainment structures were larger and more numerous in the $b$ = 20% flow compared to the flows containing $b \leq 10\%$. Packets of cohesive sediment were seen detaching from the heads of the $b \leq 20\%$ flows, before being thrown over or under the head (Fig. 3a).

The heads of the $b$ = 35% to $b$ = 65% flows had a rounded shape with a blunt nose. These flows also produced the two-layer flow structure; hydroplaning was observed only up to $b$ = 55% (Fig. 3c–f). An increasing color difference between the two layers made the boundary between the zones more distinct as $b$ increased, while mixing with the ambient water in zone 2 reduced.

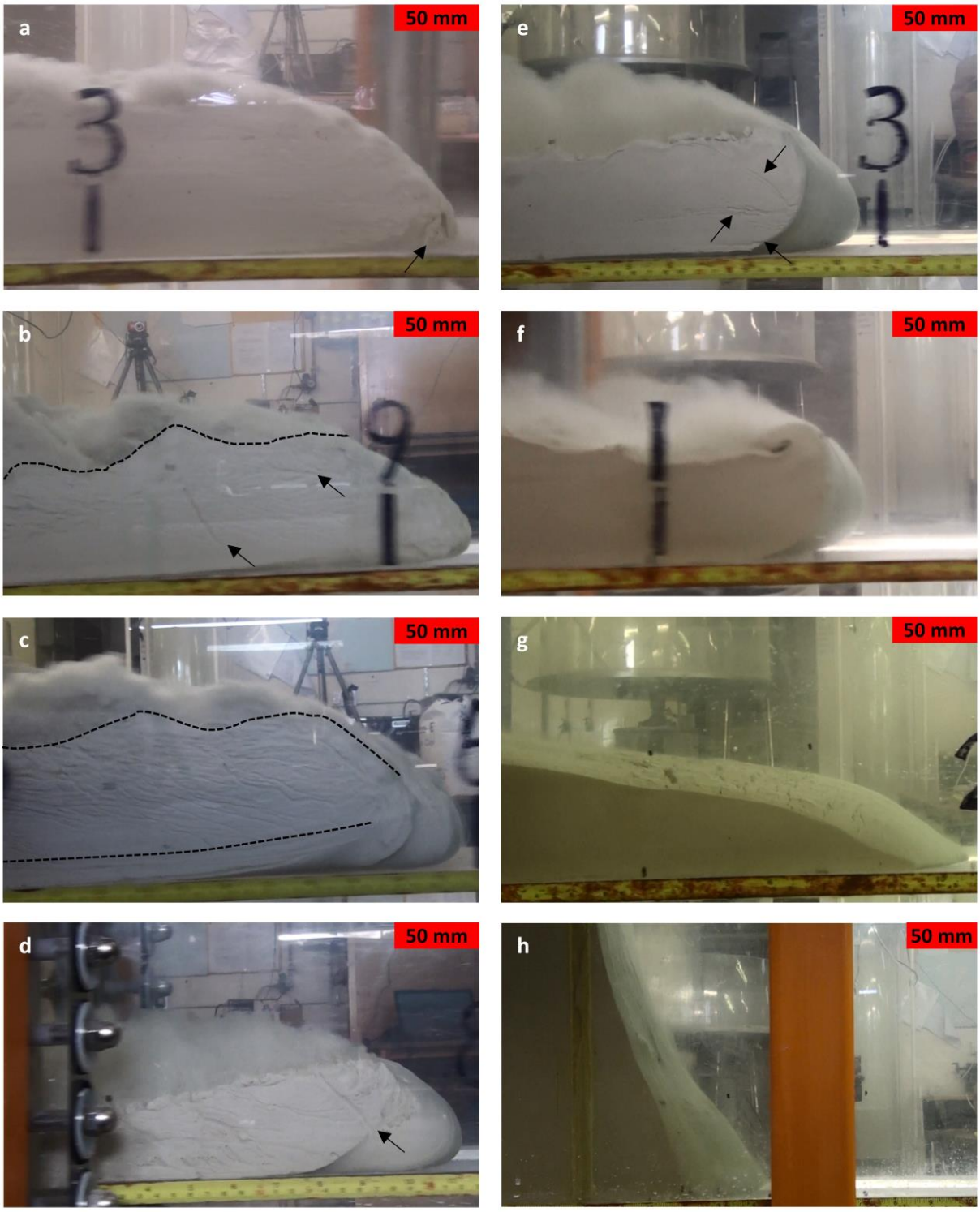


***Figure 3**: Video snapshots of the heads of the mixed-clay flows. (a) Fully turbulent b = 0% flow, at t = 3.24 s and x = 1.10 m; a packet of cohesive sediment is shown by the arrow. (b) Pointed*

*head of the b = 20% weak high-density turbidity current, which can be divided into two parts shown by the dotted line, at t = 7.00 s and x = 2.81 m; coherent fluid entrainment structures are visible in the lower layer and shown by arrows. (c) b = 35% flow, at t = 4.63 and x = 1.79 m; this strong high-density turbidity current can be divided into three parts, shown by the dotted lines (see main text). (d) Rounded head of the b = 45% flow, at t = 6.80 s and x = 2.39 m; mixing in the upper layer is reduced and the arrow points to bubbles in lower zone 1. (e) Hydroplaning head of the b = 55% flow, with a few thin coherent fluid entrainment structures shown by arrows, at t = 2.80 s and x = 0.89 m. (f) Mud flow at b = 65%, at t = 1.57 s and x = 0.43 m; the head of the flow is curled back on itself. (g) Featureless, wedge-shaped head of the b = 85% mud flow with tension cracks on the surface, at t = 3.73 s and x = 0.58 m. (h) Front of the b = 100% slide, at t = 5.06 s and x = 0.11 m.*

The head of the $b$ = 35% flow initially had a two-layer structure, but from $x$ = 1.06 m to $x$ = 2.30 m the flow could be divided into three layers: (i) a thin, dense lower zone 1a, which contained horizontal coherent fluid entrainment structures; (ii) a thick, dense middle zone 1b with many angled coherent fluid entrainment structures; and (iii) a thin, dilute upper zone 2, dominated by mixing with the ambient water (Fig. 3c). Zone 1a became featureless after $x$ = 2.30 m and the coherent fluid entrainment structures in zone 1b started to reduce in number and thin until by $x$ = 3.20 m the flow reverted to a two-layer structure with a featureless zone 1.

Within the bipartite structure of the $b$ = 45% flow, striking horizontal coherent fluid entrainment structures formed in the dense lower layer at $x$ = 0.75 m, which were angled from $x$ = 1.10 m to $x$ = 3.05 m, after which the coherent fluid entrainment structures ceased to exist (Fig. 3d). From $x$ = 3.43 m, bubbles appeared in the head of the $b$ = 45% flow. During the final flow stage, the bubbles became elongated as the head of the flow stretched. In the head of the $b$ = 55% flow, the

dense lower layer was mostly featureless apart from a few, thin coherent fluid entrainment structures from $x$ = 0.60 m to $x$ = 1.65 m (Fig. 3e).

Upon leaving the reservoir, the top of the head of the $b$ = 65% flow curled back on itself, producing a rounded head with a curl at the top (Fig. 3f) until $x$ = 1.20 m, when the curl became indistinct from the rest of the head. The head of the $b$ = 65% flow did not hydroplane. The dense lower zone was featureless until $x$ = 0.90 m, when bubbles developed in the head of the flow which lasted for the flow duration. In the final flow stages, small tension cracks perpendicular to the flow direction appeared.

The $b$ = 75% and $b$ = 85% flows had pointed, wedged-shaped heads without internal features (Fig. 3g). The $b$ = 75% flow hydroplaned at the start and produced a weak suspension cloud at its upper boundary as it travelled along the tank. In contrast, the front of the head of the $b$ = 85% flow did not hydroplane or mix with the ambient water (Fig. 3g). Tension cracks developed during the final flow stages of both flows; the tension cracks were greater in size and number for the $b$ = 85% flow than for the $b$ = 75% flow. The highest bentonite fraction flow, $b$ = 100%, left the reservoir *en-masse* without a discernible head, mixing, or hydroplaning (Fig. 3h). Vertical tension cracks, parallel to the flow direction developed at the front of the flow.

### 3.1.2 Flow velocity and run-out distance

The head of the flows accelerated rapidly once the lock gate was lifted (Fig. 4a). The maximum head velocity, $U_h$, increased slightly from 0.43 m s$^{-1}$ for the $b$ = 0% flow to 0.45 m s$^{-1}$ for the $b$ = 10% and $b$ = 20% flows. Thereafter, further increases of the bentonite fraction in the flow reduced the maximum head velocity, eventually reaching a minimum of $U_h$ = 0.07 m s$^{-1}$ for $b$ = 100% (Fig. 4a, Table 1). Velocity fluctuations of up to 0.1 m s$^{-1}$ were observed as the flows travelled along the tank.

After the initial acceleration, the $b$ = 0% to 20% flows maintained a fairly constant head velocity until *c.* 3 m; thereafter these flows started to decelerate to *c.* 50% of $U_h$ before reflecting off the end of the tank. In contrast, the flows with $b \geq 35\%$ showed a shorter period of steady flow velocity before deceleration started. These flows exhibited a rapid decrease in velocity in the final flow stages to produce a measurable runout distance. The head velocity of the $b$ = 100% flow behaved differently to the other flows, increasing rapidly to 0.07 m $s^{-1}$, before reducing to zero within 0.22 m.

All flows with $b \geq 35\%$ produced deposits with measurable run-out distances, $x_0$, that reduced from $x_0$ = 4.07 m for $b$ = 35% to $x_0$ = 0.22 m for $b$ = 100% (Fig. 4b, Table 1). The deposits of the $b$ = 35% to $b$ = 55% flows decreased steadily in thickness from the back of the reservoir to $x$ = *c.* 0.90 m, attaining a constant thickness thereafter. The $b$ = 65% and $b$ = 75% flows produced deposits that thinned from the back of the reservoir to $x$ = 0.70 m and $x$ = 0.50 m, respectively, before increasing in thickness again to produce a distinct depression in the deposits. The deposits of the $35\% \leq b \leq 75\%$ flows all had abrupt terminations with steep leading edges. The flows laden with $b$ = 85% and $b$ = 100% produced deposits which rapidly decreased from maximum thickness to zero to produce wedge-shaped and block-shaped deposits, respectively.

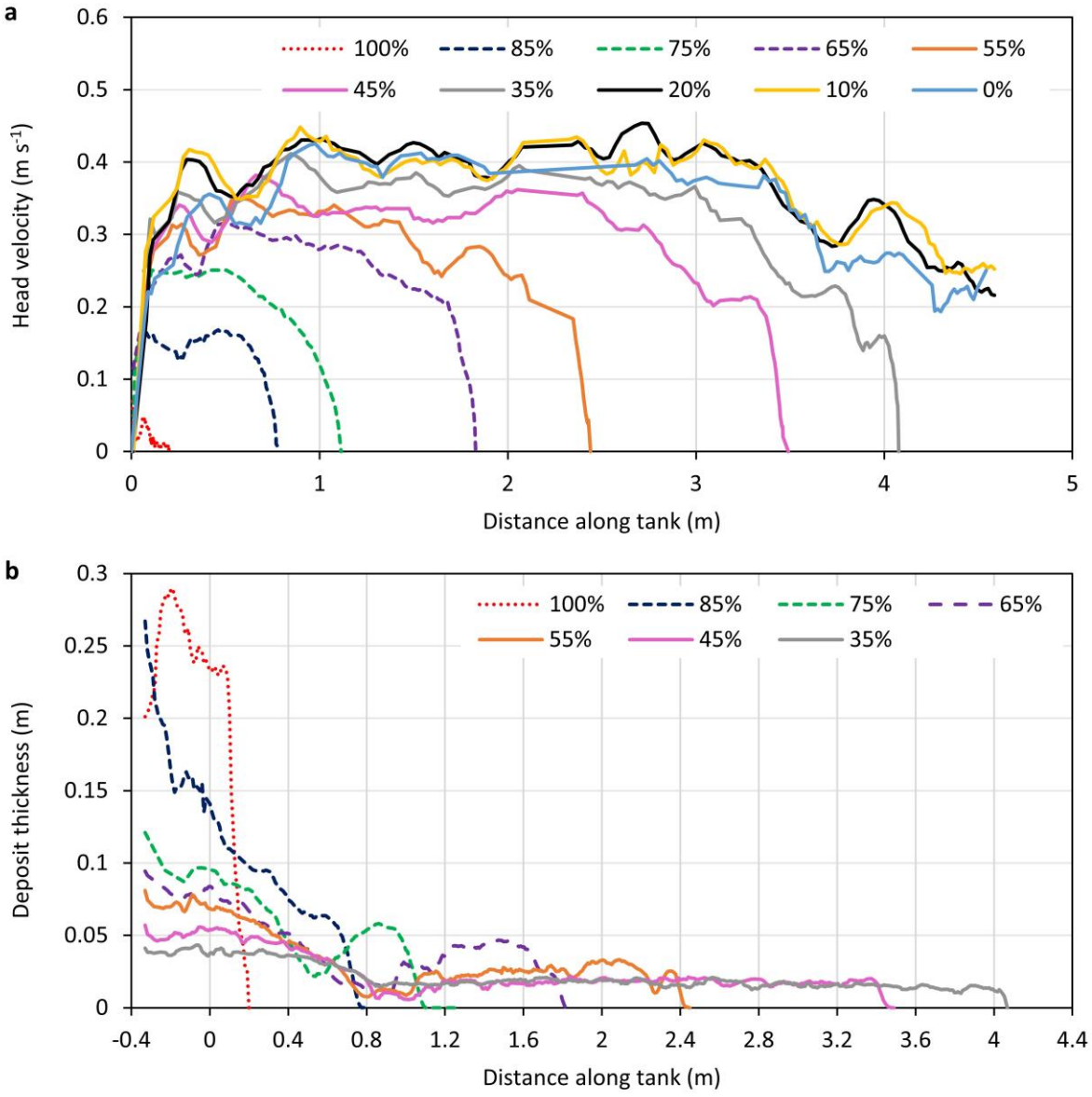


***Figure 4****: (a) Head velocity and (b) deposit thickness against distance along the tank for the mixed-clay flows. The different colors denote different bentonite fractions. The dotted, dashed, and continuous lines indicate slides, cohesive mud flows, and high-density turbidity currents, respectively.*

### 3.2 Rheology experiments

The rheological characteristics were measured for mixtures of the same composition as the starting suspensions used in the lock-exchange experiments. All three rheological tests show that the yield stress, $\tau_y$, and complex shear modulus, $G$, reduce from $b$ = 0% to 10%, with the greatest reduction for both variables shown in the oscillatory test (Fig. 5). The stress- and strain-controlled tests then show a slight increase in $\tau_y$ and $G$ from $b$ = 10% to 20%, and for $b$ > 20% the two variables increase exponentially with increasing $b$. In contrast, the $\tau_y$-values from the oscillatory test are constant for $b$ = 10% and 20%, after which $\tau_y$ increases with increasing $b$. The $G$-values from the oscillatory tests are similar for $b$ = 10% and $b$ = 20%. $G$ then increases exponentially, as $b$ increases, in the same manner as in the stress- and strain-controlled tests (Fig. 5).

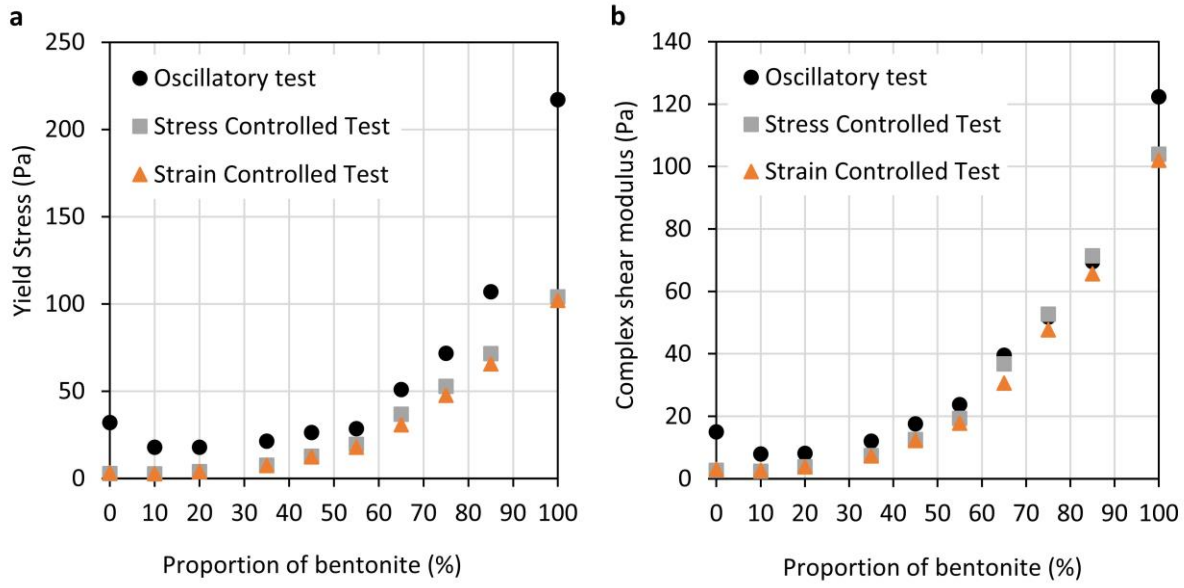


***Figure 5****: (a) Yield stress, $\tau_y$, and (b) complex shear modulus, G, of the suspensions against bentonite fraction in the suspension, b, obtained from the three rheological tests.*

## 4 Process interpretations of the mixed kaolinite–bentonite flows and deposits

### 4.1 Visual observations

The experimental SGFs in Baker et al. (2017) were subdivided into low-density turbidity currents (LDTCs), high-density turbidity currents (HDTCs), mud flows, and slides, all of which have unique flow behavior. The $0\% \leq b \leq 55\%$ flows contained a dense lower zone 1 and a dilute upper zone 2 and are classified as HDTCs (sensu Lowe, 1982; cf. Baker et al., 2017). The darker zone 1 has a high clay concentration as a result of the settling of clay particles towards the base of the flow. At these concentrations, the clays collide, flocculate, and form a gel, which suppresses the turbulence in zone 1. The dilute, upper zone 2 forms by shear-induced mixing of sediment with the ambient water. The difference in color suggests a break in density. As $b$ was increased to 55%, the boundary between the two zones became more distinct, as zone 2 became progressively lighter; this is because the increasing cohesive forces in zone 1 prevented the bonds between the clay particles from breaking on a large scale.

The HDTCs can be further subdivided into weak HDTCs for $0\% \leq b \leq 20\%$ and strong HDTCs for $35\% \leq b \leq 55\%$ flows (Table 1). This classification is based on several aspects of the flow behavior linked to the cohesive strength of the flows. The $b \leq 20\%$ flows had semi-elliptically shaped heads, suggesting that these flows did not have enough cohesive strength to resist being streamlined by the hydrodynamic pressure at the flow front (Britter & Simpson, 1978; Kneller & Buckee, 2000; Middleton & Hampton, 1973). In contrast, the $35\% \leq b \leq 55\%$ flows had rounded heads, as they had enough cohesive strength to maintain their shape. The weak HDTCs ($b \leq 20\%$) did not have enough cohesive strength to initially develop the two-layer structure. The $35\% \leq b \leq 55\%$ flows had a high enough cohesive strength to resist turbulent mixing from the onset of flow, as they formed the two-layer structure directly after leaving the reservoir.

All the HDTCs contained coherent fluid entrainment structures in zone 1, which suggests that zone 1 had a yield stress great enough to limit turbulent mixing of water entrained into the flow. The coherent fluid entrainment structures became more distinct and increased in number from $b$ = 0% to 35%, signifying that the turbulence in zone 1 decreased and water inside the flow was less readily mixed into the flow. In the strong HDTCs with $b$ = 45% to 55%, the coherent fluid entrainment structures were thin and scarce, which suggests that the cohesive strength of zone 1 was high enough to limit their formation. The orientation of the coherent fluid entrainment structures in the HDTCs is interpreted as mimicking dominant flow patterns. Hence, horizontal flow in the strongly cohesive part of zone 1 formed horizontal coherent fluid entrainment structures, and the angled coherent fluid entrainment structures occurred in slightly weaker parts of zone 1, where the water can escape in an upward direction. The featureless zone 1 observed along most of the transport path of the $b$ = 55% flow, and in the final flow stages of all the flows with $b \leq 55\%$, suggests the cohesive strength of zone 1 was too great for the formation of coherent fluid entrainment structures. The presence of bubbles in the head of the $b$ = 45% flow indicates that water entrained into the flow cannot escape because of the high yield stress of the suspension.

The $0\% \leq b \leq 55\%$ and $b$ = 75% flows all hydroplaned along part of their flow path. This suggest that: (1) the dynamic pressure of the ambient fluid below the head of the flow exceeded the weight of the flow head (Mohrig et al., 1998); and (2) the permeability at the base of the flow was low enough to prevent mixing of the overridden water (Talling, 2013). The $b$ = 85% and 100% flows lacked hydroplaning, presumably because either the flow velocity was too low, or the weight at the front was too large for the hydrodynamic pressure to support the head. It is not clear why the $b$ = 65% flow did not hydroplane, as it was faster and less dense than the $b$ = 75% flow, which did hydroplane.

The 65% ≤ $b$ ≤ 85% flows are classified as mud flows (Baker et al., 2017). A strong clay gel is interpreted to have formed at these bentonite fractions. The yield stress of these gels was high enough to fully suppress the turbulence and produce a plug flow. The limited mixing at the upper boundary further confirms that these flows had a high yield stress, which prevented the clay minerals from breaking away from the main body of the flow. The bubbles in the head of the $b$ = 65% flow suggest that the gel was weak enough to allow some entrainment of water but too strong for the water to mix further into the flow. The curled head of the $b$ = 65% flow was shaped by the ambient water moving backward over the top of the head. This created a fold that could be maintained along the flow path because of the high cohesive strength of the flow. The thin, pointed head of the flows with $b$ = 75% and $b$ = 85% were also cohesive enough to resist the hydrodynamic forces. Tension cracks formed in all the cohesive mud flows, and the size and number of the tension cracks increased, as $b$ increased. The formation of tension cracks implies that the flows had a high enough yield stress to have tensile strength, placing the flows under tension. The $b$ = 100% flow is classified as a slide, as it left the reservoir as a coherent mass without substantial internal deformation (Martinsen, 1994; Mohrig & Marr, 2003). The vertical tension cracks parallel to the flow direction, suggesting perpendicular tension, were likely caused by the flow travelling faster in the center than along the sidewalls of the tank.

### 4.1 Flow velocity and run-out distance

The fixed volume concentration mixed-clay flows had a constant density difference with the ambient water upon leaving the reservoir, which controls the flow velocity. Thus, the changes in head velocity as a function of $b$ can be explained by the balance between the turbulent and cohesive forces, which in turn promotes or hinders the mobility of the flow. The maximum head velocity increased slightly from $b$ = 0% to 10% and then remained constant from $b$ = 10% to 20% (Fig. 6a).

This suggests that the turbulent forces driving the flow increased marginally from $b$ = 0% to 10% and remained constant for the flows carrying $b$ = 10% and 20%. The flows with $b$ > 20% showed a reduction in the maximum head velocity, as the bentonite fraction in the flow increased (Fig. 6a). This reduction in maximum head velocity is interpreted to result from the cohesive forces increasingly dampening the turbulent forces, resulting in the bulk settling of the clay gel and reducing the head velocity. Flows with $b$ = 35% to 100% all exhibited a rapid deceleration to zero velocity in their final flow stages (Fig. 4). This can be attributed to the positive feedback mechanism described as "cohesive freezing" by Mulder and Alexander (2001). Cohesive freezing is interpreted to occur in these experiments because of a reduction in the head velocity, which decreases turbulent forces, allowing the clay minerals to form a greater number of electrostatic bonds, in turn increasing cohesive strength. This then further reduces the turbulence and results in a rapid further reduction in the head velocity. This negative feedback loop repeats itself until the flow swiftly comes to a halt.

The run-out distance of the $b \geq 35\%$ flows decreases linearly with $b$ (Fig. 6b, $R^2$ = 0.97). This agrees with the above-mentioned increasing dominance of cohesive forces, as the bentonite fraction in the flow increased, causing the bulk settling of the flows to occur progressively closer to the lock gate. The character of the measurable deposits changed for from wedge-shaped with an extension ($35\% \leq b \leq 55\%$), via wedge-shaped with a distinct depression ($b$ = 65% and $b$ = 75%), to wedge- or block-shaped ($b$ = 85% and $b$ = 100%, respectively). The changes in deposit signature as the bentonite fraction in the flow increased are interpreted to characterise increasing cohesive forces in the flow encouraging bulk settling of clay gels closer to the reservoir, in an analogous way to the pure clay deposits of Baker et al. (2017).

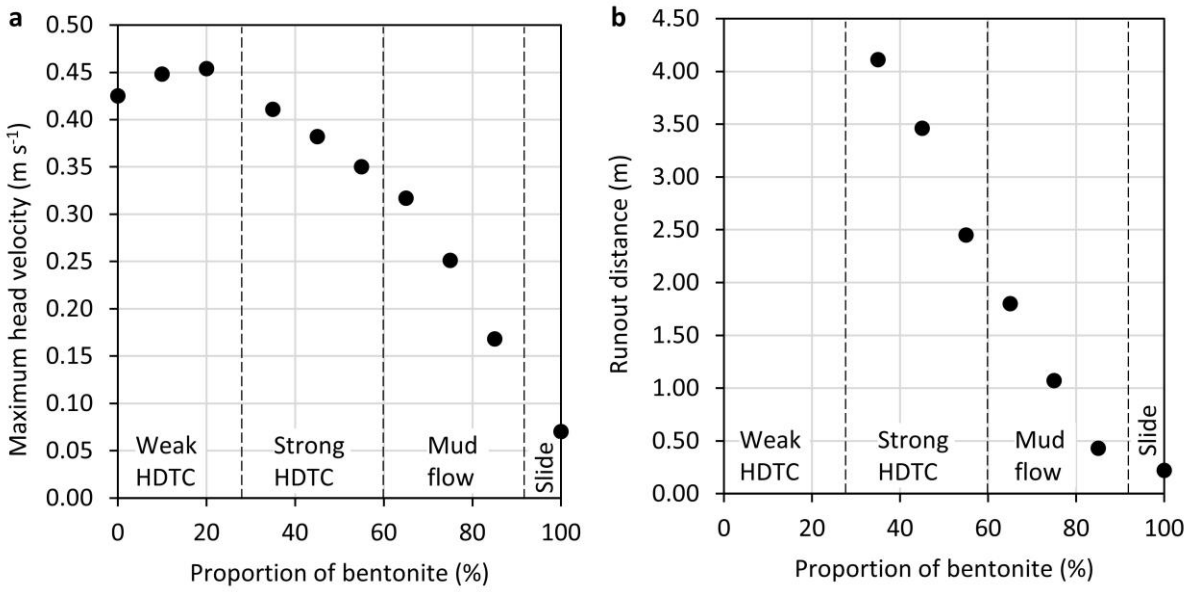


***Figure 6:*** *(a) Maximum head velocity and (b) run-out distance against bentonite fraction in the sediment gravity flow, with the boundaries between the flow types (determined as the middle bentonite fraction between bentonite fraction values where flow type changed). HDTC = high-density turbidity current.*

## 5 Discussion

### 5.1 Effect of clay mineral mixture on suspension rheology, flow behavior, head velocity, and run-out distance

The experimental data show that flow mobility initially increased as the fraction of bentonite increased from $b = 0\%$ to $b = 10\%$ and only started to decrease for $b > 20\%$. The reduction in flow mobility, as $b$ increased above 20%, is expressed by a progressive reduction in maximum head velocity, $U_h$, for $b > 20\%$ and progressively shorter run-out distances, $x_0$, for $b \geq 35\%$ (Fig. 6). The flow type also changes from weak HDTC, via strong HDTC and mud flow, to slide, as $b$ increased, suggesting an increasing dominance of cohesive over turbulent forces. All these high-density clay flows formed a clay gel in the dense lower layer or along the entire flow height, defined as a

volume-filling network in which all the clay minerals are connected by attractive bonds (Ali & Bandyopadhyay, 2016; Baas et al., 2009; Lowe & Guy, 2000). The observed reduction in flow mobility, as progressively more kaolinite is replaced by bentonite, results from the ability of the strongly cohesive bentonite minerals to increase the cohesive forces in the clay gel and dampen the turbulent forces driving the flow.

The rheological data provide direct evidence for increasing the cohesive strength in the starting suspensions with greater *b*, demonstrated by the increasing yield stress and complex shear modulus of the $b \geq 20\%$ suspensions (Fig. 5). These rheological trends match previous work on mixed kaolinite–bentonite suspensions at fixed volume concentrations. At low-volume concentrations of *c.* 2% and 0.1%, Kasperski et al. (1986) and Keren (1989) found that replacing kaolinite with bentonite increased the apparent viscosity. At the other extreme of high-volume concentrations, replacing kaolinite with bentonite in kaolinite–bentonite pastes increased the liquid limit, defined as the water content at which material changes from a plastic to liquid state (Grabowska-Olszewska, 2003; Karunaratne et al., 2014; Lagaly, 1989). At volume concentrations of *c.* 6%, Au and Leong (2013) found that increasing the bentonite fraction increased the yield stress of the suspensions.

Increasing the bentonite fraction in the suspensions increases their cohesive strength by increasing the strength and number of inter-particle bonds within the clay gels. Bentonite is a strongly cohesive clay mineral owing to its small size, large specific surface area, and high cation exchange capacity (Yong et al., 2012). Thus, if bentonite is added to the suspension in place of weakly cohesive kaolinite, the strength of the inter-particle forces increases, producing larger yield stresses (Au & Leong, 2013; Lagaly, 1989). Replacing kaolinite with bentonite also increases the number of inter-particle bonds in the gels as bentonite swells and delaminates, increasing the particle

concentration. The distinctive swelling of bentonite occurs because of adsorption of water into the interlayer space in the clay minerals. This allows the minerals to expand and swell to 10 times their dry volume (Au & Leong, 2013; Murray, 1991). If the interlayer spacing expands greatly, the bentonite layers are able to delaminate into individual or thin packets of silicate layers (Lagaly & Ziesmer, 2003). The increased particle concentration by bentonite delamination results in a greater number of particle-particle bonds within the gel structure, strengthening it and increasing the yield stress (Au & Leong, 2013). Delamination also increases the strength of the particle–particle interaction, as it reduces the particle size and increases the specific surface area (Au & Leong, 2013). The replacement of weakly cohesive kaolinite by strongly cohesive bentonite may also strengthen the microstructural arrangement of the suspensions. The microstructure of bentonite–kaolinite mixtures has been inferred to change from a "card-house" to a "card-pack" structure, as the bentonite fraction is increased (Lagaly, 1989). This change in microstructure is expected to increase the yield stress (Lagaly, 1989; Nasser & James, 2009; Ndlovu et al., 2011).

The maximum head velocity of the SGFs increased as the fraction of bentonite changed from $b$ = 0% to 10% and $U_h$ only started to decrease for $b$ > 20% (Fig. 6). This is matched by a reduction in the yield stress and complex shear modulus from $b$ = 0% to 10% for all three rheology tests (Fig. 5). These rheology measurements of the strength of the clay suspension suggest that adding a small amount of bentonite to a kaolinite-dominated suspension reduces the strength of the clay gel, which was unexpected given the strongly cohesive properties of bentonite. This demonstrates that suspensions composed of mixtures of clay mineral types can have complex rheology. The strength of a clay gel is controlled not only by the strength of the particle–particle interactions but also by the microscopic arrangements of the platelets in the gel (Ali & Bandyopadhyay, 2016; Laxton & Berg, 2006; Ndlovu et al., 2011). These experimental results suggest that a small amount of

bentonite within a predominately kaolinite gel reduces the gel strength by either reducing the strength or number of the inter-particle forces or changing the microstructural arrangement of the platelets.

Possible mechanisms responsible for the reduction in yield stress, as the bentonite fraction changes from $b$ = 0% to 10%, are discussed below, but it should be noted that these mechanisms may occur concurrently and thus interactively. The first mechanism considers the change in the pH of the suspensions from an acidic pH of 4.3 at $b$ = 0% to a neutral pH of 7.1 at $b$ = 10%, which is concurrent with the reduction in suspension yield stress (Table 1). Kaolinite particles have a permanent negative charge from isomorphic substitution and also a pH-dependent charge (Au & Leong, 2013; Cruz et al., 2013). The increase in pH of the suspension from pure kaolinite to mixed kaolinite–bentonite at $b$ = 10% could cause some or all of the kaolinite edges to switch to negatively charged (Au & Leong, 2013; Tombácz & Szekeres, 2006). This would change the dominant particle interactions from strong Coulomb attraction between the positive edges and the negative faces of the kaolinite particles to weaker van der Waals attraction between the fully negatively charged kaolinite particles, thus reducing the yield stress of the $b$ = 10% suspension (Nasser & James, 2009). The large difference in particle sizes of the kaolinite and bentonite particles may also influence the number of inter-particle forces and reduce the yield stress of the $b$ = 10% suspension. Small bentonite particles may be adsorbed onto relatively large kaolinite particles, or kaolinite particles may shield bentonite particles from forming inter-particle bonds (Au and Leong, 2013; Kasperski et al., 1986). Finally, Shakeel et al. (2021) also found a reduction in complex modulus and yield stress when small amounts of kaolinite were replaced by bentonite in kaolinite–bentonite suspensions of 10–25 weight % with deionized water (their Figs 6 and 7). These changes were interpreted to result from an increase in the salt concentration of the solution

caused by salt impurities in the bentonite, which encourages particle-particle interactions (Luckham and Rossi, 1999; Shakeel et al., 2021). However, this explanation cannot be applied to the present rheology experiments conducted with salt water. Whilst more research is needed to verify the particle configuration and particle interactions in mixed kaolinite–bentonite suspensions (Au & Leong, 2013; Shakeel et al., 2021), the next section quantitatively considers the strength of the interaction between the clays in the present experiments.

### 5.2 Predictive equations for pure-clay flows applied to the mixed-clay flows

Using the same experimental set-up and dimensional analysis for pure-clay flows of kaolinite and bentonite, Baker et al. (2017) showed that the oscillatory yield stress based on the concentration of clay can be used to predict the maximum head velocity and run-out distance of the flows. Here, these pure-clay flow equations (A1-A3 in the Appendix) are adapted to test whether the oscillatory yield stresses, $\tau_y$, maximum head velocities, $U_h$, and run-out distances, $x_0$, for the mixed kaolinite–bentonite suspensions can be predicted from the pure-clay constituents, and to examine the nature of the interaction between the clay components.

Ideally for this analysis, all three quantities should be described over the complete range of bentonite fractions in the mixed-clay flows ($0 \leq b \leq 100\%$). However, for $0 \leq b \leq 20\%$, the flows reflected off the end wall and thus $x_0$ is not listed in Table 1. Baker et al.'s (2017) predictor, Equation A3, can be used directly to determine that $x_0 = 4.79$ m for $b = 0\%$, but this equation in an unmodified form cannot be used to determine $x_0$ for the $10 \leq b \leq 20\%$ mixed-clay flows.

In order to judge the $\tau_y$, $U_h$ and $x_0$ predictors for clay mineral mixtures objectively, the differences between the predicted values and the experimental data at $b = 0\%$ and 100% were quantified, as these predictors were based on pure-bentonite and kaolinite SGFs that included the 20% volumetric concentration used herein (see section A1). The percentage differences between the

measured and predicted values of $\tau_y$, $U_h$ and $x_0$ for $b$ = 0% and 100% are interpolated over the complete range of $b$ to provide acceptable ranges, which the methods of determining these quantities can be judged against. The different methods for determining the yield stress of the mixtures will be presented first, before considering the effectiveness of these methods to predict the maximum head velocity and run-out distance of mixed-clay flows.

### 5.2.1 Determining yield stress of mixed-clay suspensions from single-clay predictors

Based on the single-clay predictors, there are two distinct methods of determining the yield stress of mixed kaolinite–bentonite suspensions that characterize the interaction between the clays: linear and non-linear. The linear yield stress, representing the case of no interaction between the two clays, is based on calculating the yield stress for the kaolinite and bentonite separately and then adding the two results together (Section A2). The linear yield stress, $\tau_{yl}$, is (Equation A4):

$$\tau_{yl} = \begin{cases} \tau_{ym}\dfrac{\Delta^3(1-b)^3+b^3}{b_m^3}, & 0 < b \le b_m, \\ \tau_{ym}\dfrac{\Delta^3(1-b)^3+b_m^3}{b_m^3} + (\tau_{y0}-\tau_{ym})\left(\dfrac{b-b_m}{b_0-b_m}\right)^3, & b_m < b \le 1, \end{cases} \quad (1)$$

where $\Delta = 16/22 = 0.727$ effectively scales down the less cohesive kaolinite, so it is equivalent to the more cohesive bentonite, and $b_m$ = 80% and $b_0$ = 102.5% are the bentonite fractions corresponding to $\tau_{ym}$ and $\tau_{y0}$. Here, $\tau_{ym}$ = 37.9 Pa and $\tau_{y0}$ = 271 Pa are the yield stresses for which the maximum head velocity is highest and the run-out distance is extrapolated to be zero, respectively, which are common to both the kaolinite and bentonite pure-clay flows, but occur at different volumetric concentrations (Section A1). In Equation 1, $\tau_{ym}\Delta^3(1–b)^3/b_m^3$ determines the yield stress of kaolinite and the rest of the expression determines the yield stress of bentonite.

The non-linear yield stress, $\tau_{yn}$, allows an interaction between the clays to be represented. This is achieved by determining an equivalent enhanced bentonite fraction, $e = \Delta(1–b)+b$, that represents the combined cohesion of the kaolinite, $\Delta(1–b)$, and bentonite, $b$, used in the yield stress calculation, as explained in Section A2. The non-linear yield stress, $\tau_{yn}$, is (Equation A5):

$$\tau_{yn} = \begin{cases} \tau_{ym}\left(\dfrac{e}{b_m}\right)^3, & \Delta < e \le b_m, \\ \tau_{ym} + (\tau_{y0} - \tau_{ym})\left(\dfrac{e - b_m}{b_0 - b_m}\right)^3, & b_m < e \le 1, \end{cases} \tag{2}$$

which gives the same values as Equation 1 for $b = 0$ and $b = 100\%$. The $e$ in the numerator of Equation 2 for $e \le b_m$, if expanded, gives $e^3 = \Delta^3(1–b)^3+b^3+$ [additional terms involving both $\Delta(1–b)$ and $b$], whereas the numerator of Equation 1 for $b \le b_m$ is simply $\Delta^3(1–b)^3+b^3$. It is these additional terms in $e$, involving both the equivalent kaolinite fraction, $\Delta(1–b)$, and the fraction of bentonite, $b$, that give rise to the non-linearity representing interaction between the clays.

Figure 7a shows the linear and non-linear yield stresses against the bentonite fraction. Based on the acceptable range (thin shaded grey region in Fig. 7a), both methods agree with the data at $b = 0$ and $b = 100\%$, as expected. The linear yield stress is always below the non-linear yield stress and the observed data largely are between these two limiting cases. The linear yield stress decreases with increasing $b$ up to 38%. Figure 7b shows that this is because the kaolinite part of $\tau_{yl}$ in Equation 1, for $b < b_m$, $\tau_{ym}\Delta^3(1–b)^3/b_m^3$, decreases more quickly than the bentonite part of $\tau_{yl}$, $\tau_{ym}b^3/b_m^3$, increases. For $0 \le b < 18\%$, the data are close to the linear prediction, implying only limited cohesive interaction between the kaolinite and bentonite in this range. In other words, the observed reduction in yield stress from b = 0% to 10% may result from the fact that the increase in yield stress from the addition of 2% bentonite is smaller than the reduction in yield stress from the removal of 2% kaolinite at high kaolinite concentrations. However, the other mechanisms

explaining the weakening cohesion in Section 5.1 may still also help explain why $\tau_{yl}$ overpredicts the observed yield stress at $b$ = 10%. For $b \geq 45\%$, the non-linear method is closer to the data than the linear method, and the fit gets increasingly better as $b$ approaches 100% ($R^2$ is larger for $\tau_{yn}$), implying a strengthening kaolinite–bentonite interaction. Thus, it seems likely that some combination of the linear and non-linear yield stresses, where the degree of non-linearity increases with $b$, most closely fits the mixed-clay yield stress data.

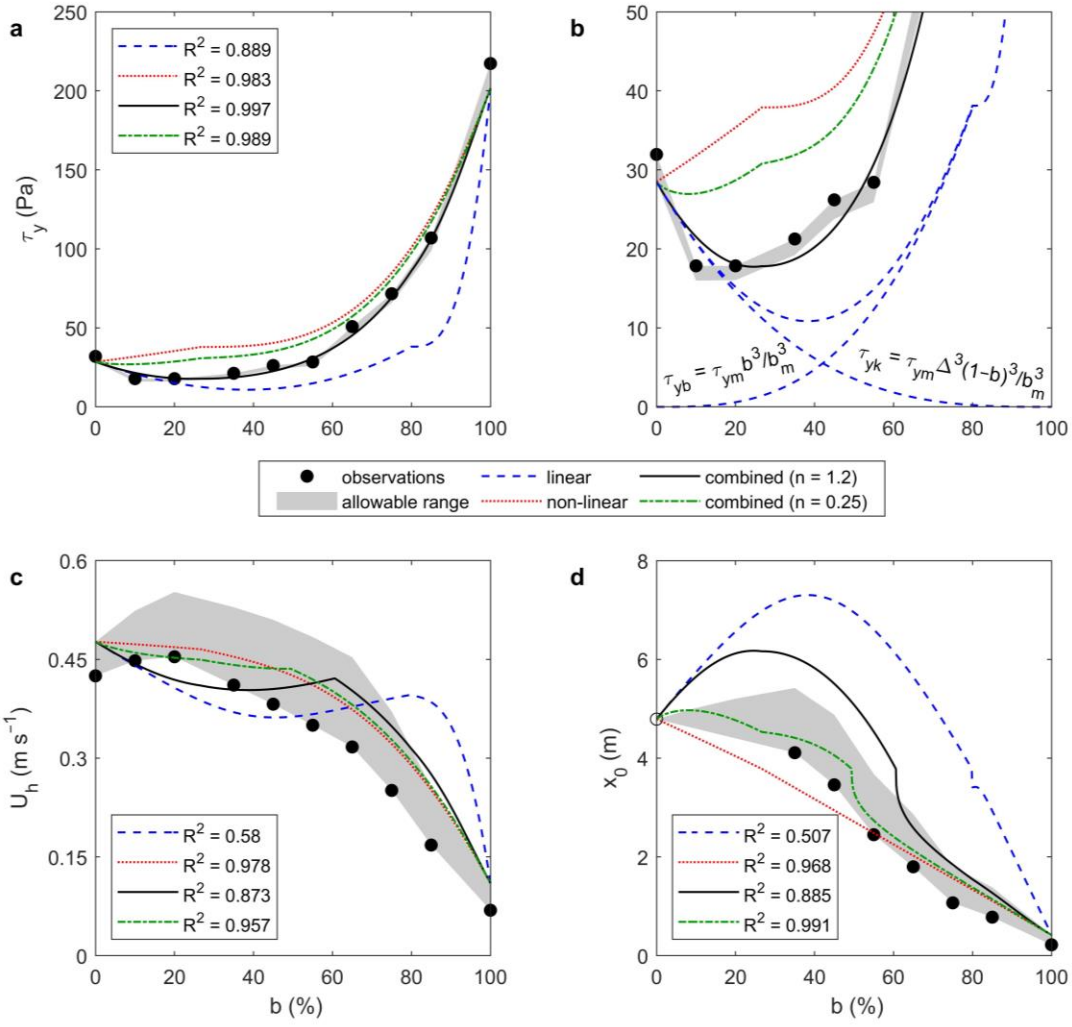

***Figure 7**: Observed (a,b) yield stress, $\tau_y$, (c) maximum head velocity, $U_h$, Equation 4, and (d) run-out distance, $x_0$, Equation 5, versus bentonite fraction, b, with allowable range and curves showing the various methods: linear ($\tau_{yl}$), Equation 1, non-linear ($\tau_{yn}$), Equation 2, and combined ($\tau_{yc}$), Equation 3, with n = 1.2 and 0.25. Central legend applies to all panels and $R^2$ values are listed for each curve. (b) is an expanded scale of (A) for $\tau_y \leq 50$ Pa, and shows the kaolinite and bentonite components, $\tau_{yk}$ and $\tau_{yb}$, of linear yield stress. In (d), $x_0$ with an open circle was estimated from Equation A3 with b = 0%.*

In order to include the appropriate amount of non-linearity compared to the observed yield stresses, a combined stress, $\tau_{yc}$, is proposed:

$$\tau_{yc} = \tau_{yl} + (\tau_{yn} - \tau_{yl})b^n, \tag{3}$$

where $\tau_{yl}$ and $\tau_{yn}$ are given by Equations 1 and 2, such that Equation 3 is linear at $b$ = 0%, non-linear at $b$ =100%, and $n$ is a weighting parameter ($n$ = 1 corresponds to equal weighting and $n$ > 1 or $n$ < 1 weight the linear or non-linear yield stress more heavily). Figure 7a shows that $\tau_{yc}$, with $n$ = 1.2 fits the data best ($R^2$ = 0.997), suggesting that this represents the correct amount of non-linearity in the yield stress.

### 5.2.2 Predicting maximum head velocity and run-out distance of mixed-clay flows

Based on an analogy with the pure-clay predictors, the maximum head velocity and run-out distance can be described by generic equations, such that the only difference between the methods is how the yield stress is calculated from the bentonite fraction, as described above. Based on Equation A2, the generic maximum head velocity ($U_{hp}$) is:

$$U_{hp} = U_{hm} \times \begin{cases} \left(\dfrac{\tau_{yp}}{\tau_{ym}}\right)^{1/6}, & 0 < \tau_{yp} \leq \tau_{ym}, \\ \dfrac{\tau_{y0} - \tau_{yp}}{\tau_{y0} - \tau_{ym}}, & \tau_{ym} < \tau_{yp} \leq \tau_{y0}, \end{cases} \tag{4}$$

where subscript $p$ describes the method used to determine $\tau_{yp}$ ($l$ = linear, $n$ = non-linear or $c$ = combined linear and non-linear, Equations 1, 2 or 3) and $U_{hm}$ is the maximum in $U_h$ occurring at $\tau_{ym}$, given by an equally-weighted sum of the pure-clay values: $U_{hmk}+(U_{hmb}-U_{hmk})b$, with $U_{hmk}$ = 0.5 m s$^{-1}$ and $U_{hmb}$ = 0.37 m s$^{-1}$ being the maximum in $U_h$ for kaolinite and bentonite, respectively (Baker et al., 2017). Likewise, based on Equation A3, the generic run-out distance, $x_{0p}$, is:

$$x_{0p} = x_{0m} \times \begin{cases} 1 - \frac{2}{3}\left(\frac{\tau_{yp}}{\tau_{ym}}\right)^{1/2}, & 0 < \tau_{yp} \leq \tau_{ym}, \\ \frac{1}{3} - \frac{1}{3}\left(\frac{\tau_{yp} - \tau_{ym}}{\tau_{y0} - \tau_{ym}}\right)^{1/3}, & \tau_{ym} < \tau_{yp} \leq \tau_{y0}, \end{cases} \quad (5)$$

where $x_{0m}$ = 11.35 m is the maximum run-out distance of both pure-clay suspensions (Baker et al., 2017).

The results of the different methods for determining the maximum head velocity and run-out distance, using Equations 4 and 5, are compared with the observations in Figs 7c and 7d. Compared to the observed maximum head velocity: (i) the linear curve agrees if $0 \leq b < 9\%$ and $50 < b < 73\%$ (32% of $b$), with $R^2$ = 0.58; (ii) the combined ($n$ = 1.2) curve agrees for $0 \leq b < 9\%$ and $38 < b < 80\%$ (51% of $b$), with $R^2$ = 0.873; and (iii) the non-linear curve agrees for all $b$, with the highest $R^2$ = 0.978. Compared to the observed run-out distance: (i) the linear curve never agrees ($R^2$ = 0.507); (ii) the combined ($n$ = 1.2) curve agrees for $b > 61\%$ (39% of $b$), with $R^2$ = 0.885; and (iii) the non-linear curve agrees for $b > 55\%$ (45% of $b$), with the highest $R^2$ of 0.968. By changing $n$ to 0.25 in Equation 3, which makes the weighting more strongly non-linear, the maximum head velocity and run-out distance agree for all $b$, with $R^2$ = 0.957 and 0.991, respectively. However, this corresponds to a yield stress with more non-linearity than is observed (cf., combined ($n$ = 0.25) curve in Fig. 7a, with a slightly lower $R^2$ = 0.989). None of the methods predict the maximum in

$U_h$ at $b$ = 20% seen in the data (Fig. 7c) that appears to be linked to the minimum in yield stress (Fig. 7a,b).

For 20% bentonite–kaolinite mixtures, based on combining Baker et al.'s (2017) pure-clay predictive equations linearly and non-linearly, the yield stress, maximum head velocity and run-out distance all show some degree of non-linearity, which increases with increasing bentonite fraction. For yield stress, the non-linear method is closer to the measured yield stress values than the linear method for $b \geq 45\%$, implying an increasingly strong cohesive interaction between the two clays as the bentonite fraction increases in this range. The degree of non-linearity is quantified in Equation 3 by the value of $n$, with $n = 0.25$ denoting stronger non-linearity than $n = 1.2$, so yield stress, best described by $n = 1.2$, is less non-linear than maximum head velocity and run-out distance, which are best described by $n = 0.25$. For $b < 20\%$, the closeness of the yield stress to the linear curve demonstrates that there is only limited cohesive interaction between kaolinite and bentonite for this range. However, $n = 0.25$ represents a reasonable compromise in fitting to the yield stress, maximum head velocity and run-out distance, with $R^2 \geq 0.957$ for all three parameters. Whilst $n = 1.2$ and $n = 0.25$ could be used to predict these quantities for mixtures of kaolinite and bentonite with combined volumetric concentrations other than 20%, it is unclear how generally applicable these values of $n$ are.

### 5.3 Wider implications

This study demonstrates that high-density cohesive SGFs that carry clay at the same total volume concentration can have remarkably different yield stresses, flow properties, and deposits, as a function of clay mineral proportions in the flow. The large differences in flow behavior, as the proportions of bentonite and kaolinite were changed in the present laboratory flows, builds on work comparing SGFs of single clay mineral type, to provide further evidence that knowledge of

the clay mineral composition is vital for the correct interpretation of the flow and deposit properties of natural high-density cohesive SGFs (Baas et al., 2016; Baker et al., 2017; Marr et al., 2001). The kaolinite–bentonite experiments demonstrate how the mixing of clay mineral types with different cohesive strengths can result in non-linear changes in flow behavior. The predictive equations for mixed-clay suspension yield stress developed from the pure-clay constituents further emphasizes the importance of non-linearity.

At present, the experimental results cannot be scaled up quantitatively to predict the properties of natural mixed-clay SGFs and their deposits, because these flows are often faster and more turbulent (Talling et al., 2013), which limits the formation of cohesive bonds between clay particles. Therefore, higher clay concentrations are expected to be required to produce natural HDTCs, mud flows, and slides, in which cohesive forces dominate over turbulent forces and where changes in the proportions of clay mineral types are expected to influence flow behavior. Nevertheless, the general trends observed in the experiments should still be valid in the natural environment and a qualitative comparison can be made with full-scale, natural SGFs.

Increasing the bentonite fraction from 0% to 20% in the kaolinite-dominated flows had a small but unexpected effect on the flow behavior: the maximum head velocity (or, more generally, the flow mobility) increased and the yield stress decreased (Fig. 8). This suggests that, all other factors being equal, a small fractional increase in the more cohesive clay mineral in a natural weak HDTC may decrease, rather than increase, yield stress and promote flow mobility. As the yield stress of the experimental kaolinite-bentonite flows can be predicted by the linear addition of the component clay yield stresses at low bentonite fractions (Equation 1), by definition there is very limited interaction between the clays for these weak HDTCs. Thus, the yield stress of the component clay mineral types may be added linearly to predict the starting suspension yield stress for kaolinite-

bentonite weak HDTCs. This linear addition of yield stresses is expected to also apply to lower-concentration kaolinite-bentonite flows, and other mixed-clay flows, behaving as LDTCs. In these flows, the sum of the yield stresses of the clay mineral constituents remains below the threshold for flow behavior dominated by cohesive forces. This would be particularly relevant to natural LDTCs with a total clay concentration dynamically equivalent to the ≤ 10% clay-laden turbidity currents of Baker et al. (2017), in which the mobility of the bentonite flows was similar to the kaolinite flows, despite the large difference in cohesive strength of these clay mineral types. In summary, there is scope to predict the flow and deposit properties of mixed-clay LDTCs and weak HDTCs in the natural environment from the linear addition of the rheological properties of the constituent clay mineral types.

Increasing *b* above 35% in the experiments dramatically reduced the head velocity and run-out distance of the strong HDTCs, mud flows, and slides (Fig. 8). This decrease in mobility is inferred to also apply to natural kaolinite–bentonite laden strong HDTCs, mud flows, and slides. However, the total clay concentration and *b* values, at which these flows lose velocity and attain a shorter run-out distance, can be higher than in the experiments, as natural SGFs are often faster and more turbulent (Talling et al., 2013). Since Equations 1–5 predict a dominance of non-linear interaction between kaolinite and bentonite for strong HDTCs, mud flows, and slides, linear addition of the clay mineral component yield stresses cannot be used to predict the mobility of similar natural turbulence-attenuated flows. A non-linear approach is needed, but it is unknown at present if $n$ = 1.2 and $n$ = 0.25, used in Equation 3 for the experimental flows, are also valid for natural kaolinite–bentonite laden strong HDTCs, mud flows, and slides.

The experiments thus revealed a tipping point in the behavior of mixed kaolinite-bentonite SGFs that should also apply to natural flows (Fig. 8). On the low-concentration side of the tipping point,

a weak HDTC carrying a small fraction of the strongly cohesive bentonite in the mixture is inferred to move faster than a flow of equal density that carries only weakly cohesive kaolinite. In contrast, on the high-concentration side of the tipping point, a flow that carries a larger fraction of bentonite is inferred to move slower and behave more akin to a strong HDTC, mud flow or slide. This in turn may lead to contrasting run-out distances and deposit shapes and types, e.g., turbidites versus debrites, for submarine fans on either side of the tipping point.

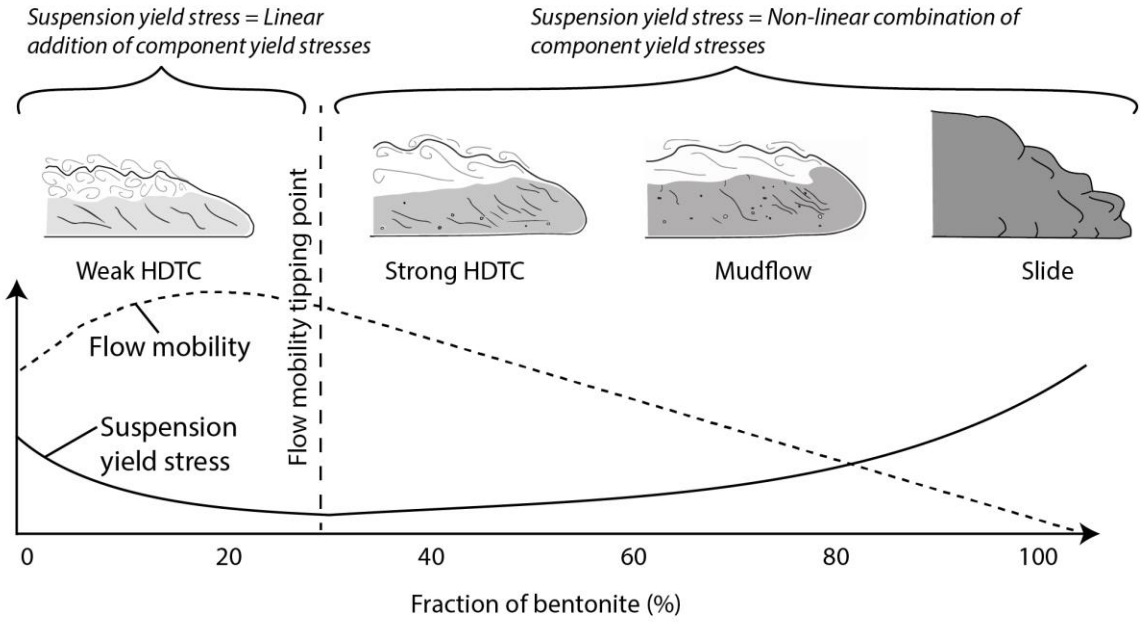


***Figure 8:*** *Summary of changing flow behavior, mobility and suspension yield stress for the experimental kaolinite–bentonite flows with increasing bentonite fraction. It is expected that natural kaolinite-bentonite flows will also go through this sequence with increasing bentonite fraction, providing the total volumetric clay concentration is large enough that cohesive forces dominate flow behavior below a bentonite fraction of 100%. Natural flows with other combinations of clay minerals may also reach a tipping point above which increasing the fraction of the more cohesive mineral rapidly reduces the flow mobility and alters flow behavior.*

For flows composed of other combinations of clay minerals with differing cohesive properties there is also likely to be a tipping point above which increasing the fraction of the more cohesive mineral results in a flow of lower mobility compared to a flow of equal density that carries primarily the weaker cohesive clay mineral type. The second most cohesive clay mineral type after bentonite is illite (Yu et al., 2014). It is likely that illite has to reach a higher fraction in the flow than bentonite before it starts to dominate the flow behavior and reach the threshold of mobility loss. Future work should investigate if illite can also significantly alter the flow behavior of mixed-clay flows if it is not the dominant clay type.

The latitudinal zonation of clay mineral production, related to contemporary climates on the continents (Biscaye, 1965; Chamley, 1986; Griffin et al., 1968; Rateev et al., 1969), may influence the behavior of cohesive-clay laden SGFs and help determine the geometry and internal architecture of mud-rich submarine fans. A literature search by Baker (2020) suggested a relationship between the latitude and dominant clay mineral type of modern, mud-rich submarine fans (Fig. 1b) that matches the global latitudinal distribution of clay mineral types in the deep ocean (Fig. 1c–f). Baker et al. (2017) inferred that high-density SGFs laden with weakly cohesive clay are more mobile and produce thinner and longer deposits than flows laden with strongly cohesive clay, assuming that all other controlling parameters are constant. However, in the natural environment, clay-rich SGFs are more likely to be composed of a mixture of different clay mineral types (e.g., Alonso & Maldonado, 1990). Therefore, to further consider the relationship between latitude, clay mineral assemblages and depositional properties of cohesive SGFs, there is a need to understand if the behavior of mixed-clay SGFs can be predicted from the dominant clay type or if knowledge of the relative contribution of the different clay mineral types is required. In the present experiments, the maximum head velocity and run-out distance of the SGFs was

significantly reduced for $b \geq 35\%$ (Fig. 6), suggesting that mixed-clay flows are sensitive to the *most cohesive* clay mineral in the flow — as opposed to the *dominant* clay mineral— once the most cohesive clay mineral has reached a fractional concentration well below 50%. This implies that future process studies of mud-rich submarine fans require knowledge of the full clay mineral assemblage, rather than relying on just the dominant clay type within these assemblages, also because the relative proportions of the different clay minerals can have a non-linear effect on the cohesive properties of the clay gels in the SGFs, thereby also effecting their mobility and deposits. It should be noted that this non-linearity may not apply to clay-rich flows of lower cohesive strength, i.e., LDTCs and weak HDTCs. The muddy deposits of these partly or fully turbulent flow types, alongside sandier deposits, are common on many mud-rich submarine fans (e.g., Spychala et al., 2017). Predictions of the dynamic behavior of the LDTCs and weak HDTCs that formed these deposits may incorporate linear addition of the yield stresses of the clay mineral fractions.

The potential influence of low fractions of strongly cohesive clay on cohesive SGF behavior may explain why the relationship between latitude and depositional properties of clay-rich flows, via changes in dominant clay mineral type, has not been perceived in metadata analyses on controls of the depositional signatures of deep-sea systems (Sømme et al., 2009). However, as detailed seafloor mapping of modern submarine fans (e.g., Maier et al., 2020) and methods of measuring clay mineral assemblages become more accessible (e.g., France-Lanord et al., 2016), efforts should be made to fully explore the relationships between climate, clay mineral production, and mud-rich submarine fan deposits.

The effect of clay mineral fractions on cohesive SGF dynamics may be more apparent in the architectural elements built by cohesive flows (e.g., strong HDTCs, mud flows, and slides) in mud-rich submarine fans and the muddy fringes of sandy deep-marine systems than in the overall

depositional style of mud-rich fans. Depositional flows dominated by cohesive forces are expected to be most common at locations where these flows decelerate, allowing the cohesive forces in the flow to dampen any remaining turbulence (Kane et al., 2017) and induce bulk settling by cohesive freezing (Mulder and Alexander, 2001), as in the experimental HDTCs and mud flows herein. These locations include lobe fringes, channel-lobe transition zones, and frontal slopes (Baas et al., 2021; Brooks et al., 2022; Spychala et al., 2017). All other factors being equal, in locations where the clay mineral assemblage has a small fraction of strongly cohesive clay compared to weakly cohesive clay, the deposits may have been produced by relatively mobile flows, such as LDTCs and weak HDTCs. These deposits are expected to be thinner with larger surface areas than deposits in which the clay mineral assemblage has a medium to large fraction of strongly cohesive clay.

It is important to note that a wide range of other factors may also influence the relationship between clay mineral fractions and the flow dynamics and deposits of laboratory and natural cohesive SGFs. For example, the sand content in a flow can influence the clay concentration required for cohesive forces to dominate the flow behavior, and thus the potential importance of clay mineral type on SGF behavior (e.g. Marr et al., 2001; Ilstad et al., 2004). The pH, temperature, inclusion of other minerals, and extent of biological cohesion can also affect interactions between clay minerals and the flow dynamics of natural mixed-clay flows (e.g. Au and Leong, 2013; Craig et al., 2020; Lin et al., 2016). Local topography and degree of confinement may greatly influence the deposit geometry of natural cohesive SGF deposits (e.g., Patacci et al., 2014). Nevertheless, this study and others (e.g., Marr et al., 2001; Baker et al., 2017) demonstrate that knowledge of the clay mineral types within natural cohesive SGFs can aid appropriate interpretation of the flow dynamics and deposits.

## 6 Conclusions

Lock-exchange experiments demonstrate that changing the proportion of clay mineral types in high-density, cohesive SGFs with a fixed total clay concentration can greatly alter the suspension rheology, flow behavior, and deposit properties. Increasing the bentonite fraction in the laboratory flows above 20% increased the yield stress of the starting suspension and reduced the head velocity and run-out distance. This decrease in mobility is expected to also apply to natural mixed-clay SGFs in which cohesive forces modulate the flow behavior, e.g., HDTCs and mud flows, and the fraction of strongly cohesive clay minerals, such as bentonite and possibly illite, increases the cohesive strength of the flow. In contrast, the laboratory flows with ≤ 20% bentonite had lower yield stresses and higher maximum head velocities than the pure kaolinite flow. This suggests that for natural flows behaving as weak HDTCs, replacing a small amount of weakly cohesive clay with more cohesive clay minerals may produce more mobile flows with longer run-out distances, as some combinations of clay minerals may reduce the suspension yield stress compared to the pure-clay suspension. Thus, mixtures of clay mineral types add complexity to the rheology of clay suspensions.

Predictive equations for the yield stress, maximum head velocity, and run-out distance of pure-clay flows were adapted for the mixed-clay flows. The yield stresses of the component clay types can be added linearly for kaolinite–bentonite laden weak HDTCs, and possibly also for LDTCs, but not for strong HDTCs, mud flows, and slides, which involve a non-linear interaction between the component clays. Non-linearity is also required to predict the maximum head velocity and run-out distance of the mixed kaolinite–bentonite flows.

The climate-controlled, latitudinal zonation of dominant clay minerals of different cohesive strength may influence the behavior of cohesive SGFs and help determine the geometry and

internal architecture of mud-rich submarine fans. Yet, natural clay-rich SGFs are rarely composed of a single clay mineral type. In the present experiments, increasing the bentonite fraction in the mixed kaolinite–bentonite flows above 35% dramatically reduced the run-out distance and head velocity of the flows. Thus, the flow dynamics of natural mixed-clay flows may be sensitive to the *most cohesive* clay mineral within the flow, even if it is not the *dominant* clay mineral. This suggests that clay mineral assemblages of natural SGF deposits should focus on full clay mineral assemblages, instead of just the dominant clay type, because the relative proportion of the different clay mineral types can have a non-linear influence on the cohesive properties of the clay suspension and its associated flow behavior and deposits.

## Acknowledgments

Equinor funded MLB's PhD studentship that enabled this research to be undertaken, using the flume facility kindly built by Bangor University technician Rob Evans. MLB was supported by a Leverhulme Trust Early Career Fellowship (ECF-2021-566). JM was funded by the European Research Council under the European Union's Horizon 2020 research and innovation program (grant no. 725955).

## Availability Statement

Lock-exchange experimental data and rheology data are supplied in the supplementary information of the manuscript for the purpose of peer review. Data is in the process of being submitted to PANGEA data repository.

## References

Ali, S., & Bandyopadhyay, R. (2016). Effect of electrolytes on the microstructure and yielding of aqueous dispersions of colloidal clay. *Soft Matter, 12*(2), 414–421. https://doi.org/10.1039/c5sm01700a

Alonso, B., & Maldonado, A. (1990). Late Quaternary sedimentation patterns of the Ebro turbidite systems (northwestern Mediterranean): Two styles of deep-sea deposition. *Marine Geology*, *95*, 353–377. https://doi.org/10.1016/0025-3227(90)90124-3

Au, P. I., & Leong, Y. K. (2013). Rheological and zeta potential behaviour of kaolin and bentonite composite slurries. *Colloids and Surfaces A: Physicochemical and Engineering Aspects*, *436*, 530–541. https://doi.org/10.1016/j.colsurfa.2013.06.039

Baas, J. H., & Best, J. L. (2002). Turbulence Modulation in Clay-Rich Sediment-Laden Flows and Some Implications for Sediment Deposition. *Journal of Sedimentary Research*, *72*(3), 336–340. https://doi.org/10.1306/120601720336

Baas, J. H., Best, J. L., & Peakall, J. (2011). Depositional processes, bedform development and hybrid bed formation in rapidly decelerated cohesive (mud-sand) sediment flows. *Sedimentology*, *58*, 1953–1987. https://doi.org/10.1111/j.1365-3091.2011.01247.x

Baas, J. H., Best, J. L., Peakall, J., & Wang, M. (2009). A Phase Diagram for Turbulent, Transitional, and Laminar Clay Suspension Flows. *Journal of Sedimentary Research*, *79*(4), 162–183. https://doi.org/10.2110/jsr.2009.025

Baas, J. H., Best, J. L., & Peakall, J. (2016). Comparing the transitional behaviour of kaolinite and bentonite suspension flows. *Earth Surface Processes and Landforms*, *41*(13), 1911–1921. https://doi.org/10.1002/esp.3959

Baas, J. H., Tracey, N. D., & Peakall, J. (2021). Sole marks reveal deep-marine depositional process and environment: Implications for flow transformation and hybrid-event-bed models. *Journal of Sedimentary Research*, *91*(9), 986–1009. https://doi.org/10.2110/jsr.2020.104

Baker, M.L. (2020) The Role of Clay Minerals in the Dynamics and Deposits of Sediment Gravity Flows. PhD Thesis, Bangor Univeristy, 257 pp.

Baker, M. L., & Baas, J. H. (2022). Does sand promote or hinder the mobility of cohesive sediment gravity flows? *Sedimentology*. https://doi.org/10.1111/sed.13072

Baker, M. L., Baas, J. H., Malarkey, J., Jacinto, R. S., Craig, M. J., Kane, I. A., & Barker, S. (2017). The Effect of Clay Type On the Properties of Cohesive Sediment Gravity Flows and Their Deposits. *Journal of Sedimentary Research*, *87*(11), 1176–1195. https://doi.org/10.2110/jsr.2017.63

Biscaye, P. E. (1965). Mineralogy and Sedimentation of Recent Deep-Sea Clay in the Atlantic Ocean and Adjacent Seas and Oceans. *Geological Society of America Bulletin*, *76*(July), 803–832. https://doi.org/https://doi.org/10.1130/0016-7606(1965)76[803:MASORD]2.0.CO;2

Britter, R. E., & Simpson, J. E. (1978). Experiments on the dynamics of a gravity current head. *Journal of Fluid Mechanics*, *88*, 223. https://doi.org/10.1017/S0022112078002074

Brooks, H. L., Ito, M., Zuchuat, V., Peakall, J., & Hodgson, D. M. (2022). Channel-lobe transition zone development in tectonically active settings: Implications for hybrid bed development. *Depositional Record*, *8*(2), 829–868. https://doi.org/10.1002/dep2.180

Chamley, H. (1986). Continental and marine paleoenvironments reflected by west Pacific clay sedimentation. *Geologische Rundschau*, *75*, 271–285. https://doi.org/10.1007/BF01770193

Craig, M. J., Baas, J. H., Amos, K. J., Strachan, L. J., Manning, A. J., Paterson, D. M., Paterson, D.M., Hope, Baker, M. L. (2020). Biomediation of submarine sediment gravity flow dynamics. *Geology*, *48*(1), 72–76. https://doi.org/10.1130/G46837.1

Cruz, N., Peng, Y., Farrokhpay, S., & Bradshaw, D. (2013). Interactions of clay minerals in copper-gold flotation: Part 1 - Rheological properties of clay mineral suspensions in the presence of flotation reagents. *Minerals Engineering*, *50–51*, 30–37. https://doi.org/10.1016/j.mineng.2013.06.003

Fagel, N. (2007). Chapter Four Clay Minerals, Deep Circulation and Climate. *Developments in Marine Geology*, *1*(07), 139–184. https://doi.org/10.1016/S1572-5480(07)01009-3

France-Lanord, C., Spiess, V., Klaus, a., Adhikari, R.R., Adhikari, S.K., Bahk, J.-J., Baxter, a. T., Cruz, J.W., Das, S.K., Dekens, P., Duleba, W., Fox, L.R., Galy, a., Galy, V., Ge, J., Gleason, J.D., Gyawali, B.R., Huyghe, P., Jia, G., Lantzsch, H., Manoj, M.C., Martos Martin, Y., Meynadier, L., Najman, Y.M.R., Nakajima, a., Ponton, C., Reilly, B.T., Rogers, K.G., Savian, J.F., Schwenk, T., Selkin, P. a., Weber, M.E., Williams, T. and Yoshida, K. (2016) Site U1454. *In* France-Lanord, C., Spiess, V., Klaus, A., Schwenk, T., and the Expedition 354 Scientists, *Bengal Fan*. Proceedings of the International Ocean Discovery Program, 354: College Station, TX (International Ocean Discovery Program). http://dx.doi.org/10.14379/iodp.proc.354.108.2016

Grabowska-Olszewska, B. (2003). Modelling physical properties of mixtures of clays: Example of a two-component mixture of kaolinite and montmorillonite. *Applied Clay Science*, *22*(5), 251–259. https://doi.org/10.1016/S0169-1317(03)00078-4

Griffin, J. J., Windom, H., & Goldberg, E. D. (1968). The distribution of clay minerals in the World Ocean. *Deep Sea Research and Oceanographic Abstracts*, *15*(April), 433–459. https://doi.org/10.1016/0011-7471(68)90051-X

Hermidas, N., Eggenhuisen, J. T., Jacinto, R. S., Luthi, S. M., Toth, F., & Pohl, F. (2018). A Classification of Clay-Rich Subaqueous Density Flow Structures. *Journal of Geophysical Research: Earth Surface*, *123*(5), 945–966. https://doi.org/10.1002/2017JF004386

Hillel, D. (2003). *Introduction to Environmental Soil Physics*. Elsevier. https://doi.org/10.1016/B978-0-12-348655-4.X5000-X

Hillier, S. (1995). Erosion, Sedimentation and Sedimentary Origin of Clays. In B. Velde (Ed.), *Origin and Mineralogy of Clays* (pp. 162–219). Berlin, Heidelberg: Springer Berlin Heidelberg. https://doi.org/10.1007/978-3-662-12648-6_4

Holtz, R. D., & Kovacs, W. D. (1981). *An introduction of geotechnical engineering*. New York: Prentice Hall.

Ilstad, T., Elverhøi, A., Issler, D., & Marr, J. G. (2004). Subaqueous debris flow behaviour and its dependence on the sand/clay ratio: A laboratory study using particle tracking. *Marine Geology*, *213*(1–4), 415–438. https://doi.org/10.1016/j.margeo.2004.10.017

Kane, I. A., Pontén, A. S. M., Vangdal, B., Eggenhuisen, J. T., Hodgson, D. M., & Spychala, Y. T. (2017). The stratigraphic record and processes of turbidity current transformation across

deep-marine lobes. *Sedimentology*, *64*(5), 1236–1273. https://doi.org/10.1111/sed.12346

Karunaratne, G. P., Chew, S. H., Lee, S. L., & Sinha, A. N. (2014). Bentonite:Kaolinite Clay Liner. *Geosynthetics International*, *8*(2), 113–133. https://doi.org/10.1680/gein.8.0189

Kasperski, K. L., Hepler, C. T., & Hepler, L. G. (1986). Viscosities of dilute aqueous suspensions of montmorillonite and kaolinite clays. *Canadian Journal of Chemistry*, *64*(9), 1919–1924. https://doi.org/10.1139/v86-316

Keren, R. (1989). Rheology of Mixed Kaolinite-Montmorillonite Suspensions. *Soil Science Society of America Journal*, *53*(3), 725–730. https://doi.org/10.2136/sssaj1989.03615995005300030014x

Kneller, B., & Buckee, C. (2000). The structure and fluid mechanics of turbidity currents: a review of some recent studies and their geological implications. *Sedimentology*, *47*, 62–94. https://doi.org/10.1046/j.1365-3091.2000.047s1062.x

Kolla, V., Kostecki, J. A., Henderson, L., & Hess, L. (1980). Morphology and Quaternary sedimentation of the Mozambique Fan and environs, southwestern Indian Ocean. *Sedimentology*, *27*, 357–378. https://doi.org/10.1007/978-981-10-2875-5_41

Lagaly, G. (1989). Principles of flow of kaolin and bentonite dispersions. *Applied Clay Science*, *4*, 105–123. https://doi.org/10.1016/0169-1317(89)90003-3

Lagaly, G., & Ziesmer, S. (2003). Colloid chemistry of clay minerals: The coagulation of montmorillonite dispersions. *Advances in Colloid and Interface Science*, *100–102*(SUPPL.), 105–128. https://doi.org/10.1016/S0001-8686(02)00064-7

Laxton, P. B., & Berg, J. C. (2006). Relating clay yield stress to colloidal parameters. *Journal of Colloid and Interface Science*, *296*(2), 749–755. https://doi.org/10.1016/j.jcis.2005.09.061

Lin, Y., Cheah, L. K. J., Phan-Thien, N., & Khoo, B. C. (2016). Effect of temperature on rheological behavior of kaolinite and bentonite suspensions. *Colloids and Surfaces A: Physicochemical and Engineering Aspects*, *506*, 1–5. https://doi.org/10.1016/j.colsurfa.2016.06.012

Lowe, D. R. (1982). Sediment Gravity Flows: II Depositional Models with Special Reference to the Deposits of High-Density Turbidity Currents. *SEPM Journal of Sedimentary Research*, *Vol. 52*, 279–298. https://doi.org/10.1306/212F7F31-2B24-11D7-8648000102C1865D

Lowe, D. R., & Guy, M. (2000). Slurry-flow deposits in the Britannia Formation (Lower Cretaceous), North Sea: A new perspective on the turbidity current and debris flow problem. *Sedimentology*, *47*, 31–70. https://doi.org/10.1046/j.1365-3091.2000.00276.x

Luckham, P. F., & Rossi, S. (1999). The colloidal and rheological properties of bentonite suspensions. *Advances in Colloid and Interface Science*, *82*(1–3), 43–92. https://doi.org/10.1016/S0001-8686(99)00005-6

Maier, K. L., Paull, C. K., Caress, D. W., Anderson, K., Nieminski, N. M., Lundsten, E., … Fildani, A. (2020). Submarine-fan development revealed by integrated high-resolution datasets from La Jolla fan, offshore California, U.S.A. *Journal of Sedimentary Research*, *90*(5), 468–479. https://doi.org/10.2110/jsr.2020.22

Marr, J. G., Shanmugam, G., & Parker, G. (2001). Experiments on subaqueous sandy gravity flows: The role of clay and water content in flow dynamics and depositional structures. *Bulletin of the Geological Society of America*, *113*, 1377–1386. https://doi.org/10.1130/0016-7606(2001)113<1377:EOSSGF>2.0.CO

Martinsen, O. (1994). Mass movements. In *The Geological Deformation of Sediments* (pp. 127–165). Dordrecht: Springer Netherlands. https://doi.org/10.1007/978-94-011-0731-0_5

Mezger, T. G. (2006). *The rheology handbook: for users of rotational and oscillatory rheometers* (2nd ed.). Hannover: Vincentz Network GmbH & Co KG. https://doi.org/https://doi.org/10.1515/9783748603702

Middleton, G., & Hampton, M. (1973). Part I. Sediment gravity flows: mechanics of flow and deposition. In: *Turbidity and Deep Water Sedimentation* (Eds G.V. Middleton and A.H. Bouma), *SEPM, Pacific Section, Short Course Lecture Notes*, 1–38. Retrieved from http://archives.datapages.com/data/pac_sepm/015/015001/pdfs/1.pdf

Mohrig, D., & Marr, J. G. (2003). Constraining the efficiency of turbidity current generation from submarine debris flows and slides using laboratory experiments. *Marine and Petroleum Geology*, *20*, 883–899. https://doi.org/10.1016/j.marpetgeo.2003.03.002

Mohrig, D., Whipple, K. X., Hondzo, M., Ellis, C., & Parker, G. (1998). Hydroplaning of subaqueous debris flows. *Bulletin of the Geological Society of America*, *110*(3), 387–394. https://doi.org/10.1130/0016-7606(1998)110<0387:HOSDF>2.3.CO

Mulder, T., & Alexander, J. (2001). The physical character of subaqueous sedimentary density flow and their deposits. *Sedimentology*, *48*(2), 269–299. https://doi.org/10.1046/j.1365-3091.2001.00360.x

Murray, H. H. (1991). Overview — clay mineral applications. *Applied Clay Science*, *5*(5–6), 379–395. https://doi.org/10.1016/0169-1317(91)90014-Z

Nasser, M. S., & James, A. E. (2009). The effect of electrolyte concentration and ph on the flocculation and rheological behaviour of kaolinite suspensions. *Journal of Engineering Science and Technology*, *4*(4), 430–446.

Ndlovu, B., Becker, M., Forbes, E., Deglon, D., & Franzidis, J. P. (2011). The influence of phyllosilicate mineralogy on the rheology of mineral slurries. *Minerals Engineering*, *24*(12), 1314–1322. https://doi.org/10.1016/j.mineng.2011.05.008

Patacci, M., Haughton, P. D. W., & McCaffrey, W. D. (2014). Rheological complexity in Sediment gravity flows forced to decelerate against a confining slope, Braux, SE France. *Journal of Sedimentary Research*, *84*(4), 270–277. https://doi.org/10.2110/jsr.2014.26

Rateev, M. A., Lisitzyn, A. P., & Nosov, G. L. (1969). The Distribution of clay minerals in the oceans. *Sedimentology*, *13*, 21–43. https://doi.org/10.1111/j.1365-3091.1969.tb01119.x

Reading, H. G., & Richards, M. (1994). Turbidite systems in deep-water basin margins classified by grain size and feeder system. *American Association of Petroleum Geologists Bulletin*, *78*(5), 792–822. https://doi.org/10.1306/A25FE3BF-171B-11D7-8645000102C1865D

Shakeel, A., Kirichek, A., & Chassagne, C. (2021). Rheology and yielding transitions in mixed

kaolinite/bentonite suspensions. *Applied Clay Science*, *211*(July), 106206. https://doi.org/10.1016/j.clay.2021.106206

Sømme, T. O., Helland-hansen, W., Martinsen, O. J., & Thurmond, J. B. (2009). Relationships between morphological and sedimentological parameters in source-to-sink systems: A basis for predicting semi-quantitative characteristics in subsurface systems. *Basin Research*, *21*(4), 361–387. https://doi.org/10.1111/j.1365-2117.2009.00397.x

Spychala, Y. T., Hodgson, D. M., Prélat, A., Kane, I. A., Flint, S. S., & Mountney, N. P. (2017). Frontal and Lateral Submarine Lobe Fringes: Comparing Sedimentary Facies, Architecture and Flow Processes. *Journal of Sedimentary Research*, *87*(1), 75–96. https://doi.org/10.2110/jsr.2017.2

Stow, D. A. V., Reading, H. G., & Collinson, J. D. (1996). Deep seas. In H. G. Reading (Ed.), *Sedimentary Environments: Processes, Facies and Stratigraphy* (pp. 395–453). Oxford, UK: Blackwell Science. https://doi.org/10.1007/978-3-319-67627-2

Talling, P.J. (2013). Hybrid submarine flows comprising turbidity current and cohesive debris flow: Deposits, theoretical and experimental analyses, and generalized models. *Geosphere*, *9*, 460–488. https://doi.org/10.1130/GES00793.1

Talling, Peter J. (2014). On the triggers, resulting flow types and frequencies of subaqueous sediment density flows in different settings. *Marine Geology*, *352*, 155–182. https://doi.org/10.1016/j.margeo.2014.02.006

Talling, Peter J., Paull, C. K., & Piper, D. J. W. (2013). How are subaqueous sediment density flows triggered, what is their internal structure and how does it evolve? Direct observations from monitoring of active flows. *Earth-Science Reviews*, *125*, 244–287. https://doi.org/10.1016/j.earscirev.2013.07.005

Thiry, M. (2000). Palaeoclimatic interpretation of clay minerals in marine deposits: An outlook from the continental origin. *Earth Science Reviews*, *49*, 201–221. https://doi.org/10.1016/S0012-8252(99)00054-9

Tombácz, E., & Szekeres, M. (2006). Surface charge heterogeneity of kaolinite in aqueous suspension in comparison with montmorillonite. *Applied Clay Science*, *34*(1–4), 105–124. https://doi.org/10.1016/j.clay.2006.05.009

Wang, Z., & Plate, E. C. H. J. (1996). A preliminary study on the turbulence structure of flows of non-Newtonian fluid. *Journal of Hydraulic Research*, *34*(April 2015), 345–361. https://doi.org/10.1080/00221689609498484

Winterwerp, J. C., & Van Kesteren, W. G. M. (2004). Introduction to the Physics of Cohesive Sediment Dynamics in the Marine Environment. In *Developments in sedimentology* (Vol. 56). Elsevier Ltd.

Yong, R. N., Nakano, M., & Pusch, R. (2012). *Environmental Soil Properties and Behaviour* (1st ed.). CRC Press. https://doi.org/10.1201/b11658

Yu, B., Yu, M., & Qi, X. (2014). Experimental Study on the Influence of Clay Minerals on the Yield Stress of Debris Flows. *Journal of Hydraulic Engineering*, *4*(April), 1–12. https://doi.org/10.1061/(ASCE)HY.1943-7900

Zhang, Q., Chen, M., Liu, J., Yu, Z., Zhang, L., & Xiang, R. (2015). Clay mineral assemblages at IODP Site U1340 in the Bering Sea and their paleoclimatic significance. *Science China Earth Sciences*, *58*(5), 707–717. https://doi.org/10.1007/s11430-014-5049-3

**Online content**

## Appendix A: Calculating linear and non-linear yield stresses for kaolinite–bentonite mixtures based on Baker et al. (2017)

### A.1 Predictive equations for pure kaolinite or bentonite suspensions

According to Baker et al. (2017), in terms of the volumetric concentration of kaolinite ($C_k$) or bentonite ($C_b$), the yield stresses ($\tau_{yk}$ or $\tau_{yb}$) are expressed generically as:

$$\tau_{yi} = \begin{cases} \tau_{ym}\left(\dfrac{C_i}{C_{mi}}\right)^3, & 0 < C_i \le C_{mi}, \\ \tau_{ym} + (\tau_{y0} - \tau_{ym})\left(\dfrac{C_i - C_{mi}}{C_{0i} - C_{mi}}\right)^3, & C_{mi} < C_i \le C_{0i}, \end{cases} \tag{A1}$$

where subscript $i$ represents either $k$ or $b$, $\tau_{ym}$ = 37.9 Pa, $\tau_{y0}$ = 271 Pa, $C_{mk}$ = 22%, $C_{mb}$ = 16%, $C_{0k}$ = 30.5% and $C_{0b}$ = 20.5%. Likewise, the maximum head velocity for kaolinite ($U_{hk}$) or bentonite ($U_{hb}$) is:

$$U_{hi} = U_{hmi} \times \begin{cases} \left(\dfrac{\tau_{yi}}{\tau_{ym}}\right)^{1/6}, & 0 < \tau_y \le \tau_{ym}, \\ \dfrac{\tau_{y0} - \tau_{yi}}{\tau_{y0} - \tau_{ym}}, & \tau_{ym} < \tau_y \le \tau_{y0}, \end{cases} \tag{A2}$$

where $U_{hmk}$ = 0.5 m s$^{-1}$ and $U_{hmb}$ = 0.37 m s$^{-1}$ and the run-out distance for kaolinite ($x_{0k}$) and bentonite ($x_{0b}$) is:

$$x_{0i} = x_{0m} \times \begin{cases} 1 - \frac{2}{3}\left(\frac{\tau_{yi}}{\tau_{ym}}\right)^{1/2}, & 0 < \tau_y \leq \tau_{ym}, \\ \frac{1}{3} - \frac{1}{3}\left(\frac{\tau_{yi} - \tau_{ym}}{\tau_{y0} - \tau_{ym}}\right)^{1/3}, & \tau_{ym} < \tau_y \leq \tau_{y0}, \end{cases} \quad \text{(A3)}$$

where $x_{0m}$ = 11.35 m. In the present experiments, $C_k$+$C_b$ = $C_t$, where $C_t$ is a constant ($C_t$ = 20%), $C_b$ = $C_t b$ and $C_k$ = $C_t$(1–$b$). Equations A1–A3 can be applied directly to the $b$ = 0 and $b$ = 100% cases: $\tau_y$ at $b$ = 0% is $\tau_{yk}$(20%) = 28.47 Pa and $\tau_y$ at $b$ = 100% is $\tau_{yb}$(20%) = 201.61 Pa; $U_h$ at $b$ = 0% is $U_{hk}$(20%) = 0.477 m s$^{-1}$ and $U_h$ at $b$ = 100% is $U_{hb}$(20%) = 0.11 m s$^{-1}$; $x_0$ at $b$ = 0% is $x_{0k}$(20%) = 4.79 m and $x_0$ at $b$ = 100% is $x_{0b}$(20%) = 0.42 m, and these values can be compared directly to those in Table 1.

To combine Equations A1–A3 for mixtures of kaolinite and bentonite in Section A2, it is first necessary to define the constants in terms of the bentonite fraction ($b$). Since $b$ = $C_b$/$C_t$, the following quantities can readily be defined: $b_m$ = $C_{mb}$/$C_t$ = 80% and $b_0$ = $C_{0b}$/$C_t$ = 102.5%. This leaves $C_{mk}$ and $C_{0k}$ in Equation A1 for $\tau_{yk}$. Since $C_t$ = 20% is less than $C_{mk}$ = 22%, only the 0 < $C_k$ < $C_{mk}$ part of Equation A1 is required for $\tau_{yk}$, so $C_{0k}$ can be ignored. In Equation A1, $C_k$/$C_{mk}$ = $C_t$(1–$b$)/$C_{mk}$ can be expressed as $\Delta$(1–$b$)/$b_m$, where $\Delta$ = $C_{mb}$/$C_{mk}$ = 16/22 = 0.727.

A.2 Combined yield stress

There are two distinct methods of determining the yield stress of mixed bentonite–kaolinite suspensions that characterise the interaction between the clays: linear and non-linear. The linear yield stress ($\tau_{yl}$) is given by $\tau_{yl}$ = $\tau_{yk}$($C_k$)+$\tau_{yb}$($C_b$) from Equation A1. With the above definitions, $\tau_{yl}$ can be expressed in terms of $b$ as:

$$\tau_{yl} = \begin{cases} \tau_{ym}\dfrac{\Delta^3(1-b)^3 + b^3}{b_m^3}, & 0 < b \le b_m, \\ \tau_{ym}\dfrac{\Delta^3(1-b)^3 + b_m^3}{b_m^3} + (\tau_{y0} - \tau_{ym})\left(\dfrac{b-b_m}{b_0-b_m}\right)^3, & b_m < b \le 1, \end{cases} \tag{A4}$$

which returns to the two pure-clay values, $\tau_{yk}(20\%)$ and $\tau_{yb}(20\%)$, at $b = 0$ and 100%, respectively. In Equation A4, $\tau_{ym}\Delta^3(1–b)^3/b_m{}^3$ determines the kaolinite part of the yield stress and the rest of the expression determines the bentonite part. Comparing the kaolinite part of the expression with the bentonite part for $b \le b_m$, $\tau_{ym}b^3/b_m{}^3$ yields that $\Delta$ effectively scales down the less cohesive kaolinite so it is equivalent to the more cohesive bentonite. Thus, $\Delta(1–b)$ is the equivalent kaolinite fraction with the same cohesion as bentonite. The non-linear yield stress takes advantage of this equivalent kaolinite fraction and combines it with the bentonite fraction to produce an enhanced equivalent bentonite fraction with the same cohesion as the kaolinite and bentonite combined, given by $e = \Delta(1–b)+b$, which can then be used in Equation A1 to produce the non-linear yield stress, $\tau_{yn}$:

$$\tau_{yn} = \begin{cases} \tau_{ym}\left(\dfrac{e}{b_m}\right)^3, & \Delta < e \le b_m, \\ \tau_{ym} + (\tau_{y0} - \tau_{ym})\left(\dfrac{e-b_m}{b_0-b_m}\right)^3, & b_m < e \le 1, \end{cases} \tag{A5}$$

which gives the same values as Equation A4 for $b = 0\%$ and $b = 100\%$ ($e = \Delta$ and 1). Notice $e$ in the numerator of Equation A5 for $e \le b_m$ gives $e^3 = [\Delta(1–b)+b]^3 = \Delta^3(1–b)^3+b^3+3\Delta^2(1–b)^2b+3\Delta(1–b)b^2$, whereas the numerator of Equation A4 for $b \le b_m$ is simply $\Delta^3(1–b)^3+b^3$. It is the additional terms in $e$ that involve both the equivalent kaolinite fraction, $\Delta(1–b)$, and the bentonite fraction, $b$, that give rise to the non-linearity in the interaction between the clays. A similar argument can be made for the difference between Equations A4 and A5 for $b$ and $e > b_m$.